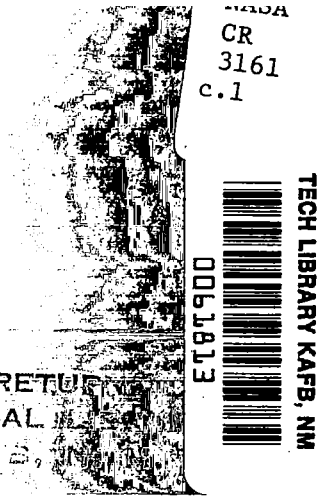

NASA Contractor Report 3161

Analysis, Design, and Test of Acoustic Treatment in a Laboratory Inlet Duct

R. E. Kraft, R. E. Motsinger,
W. H. Gauden, and J. F. Link

CONTRACT NAS1-14847
JULY 1979

NASA

NASA Contractor Report 3161

Analysis, Design, and Test of Acoustic Treatment in a Laboratory Inlet Duct

R. E. Kraft, R. E. Motsinger,
W. H. Gauden, and J. F. Link
General Electric Company
Evendale, Ohio

Prepared for
Langley Research Center
under Contract NAS1-14847

National Aeronautics
and Space Administration

Scientific and Technical
Information Branch

1979

TABLE OF CONTENTS

LIST OF ILLUSTRATIONS

LIST OF ILLUSTRATIONS (Continued)

LIST OF ILLUSTRATIONS (Concluded)

LIST OF TABLES

1.0 SUMMARY

The major objectives of this study were the design and test of a series of inlet treatment configurations. In particular, it was desired to investigate the properties of the bulk absorber material Kevlar* relative to conventional, single-degree-of-freedom (SDOF) resonator panels. The optimized designs were to include the concept of multiphasing, utilizing up to three panels in series.

Before proceeding with the design optimization analysis, it was necessary to modify the modal analysis eigenvalue search routine to eliminate the occurrence of eigenvalue problems such as double eigenvalues or missed eigenvalues. In addition, an analysis was developed to account for the acoustic effects of thin boundary layers in the mean flow.

The optimized treatment designs were accomplished using an analytical program for the prediction of acoustic wave propagation in cylindrical ducts. Input to the program was based on a preliminary measurement using the Spinning Mode Synthesizer as a sound source for the inlet duct in the Anechoic Chamber. Panel designs to achieve the desired impedance components were accomplished using the normal-incidence, standing-wave tube in the case of the bulk absorber and current analytical models in the case of the SDOF.

The treatment panels were tested in a program conducted in the NASA-Langley ANRL Anechoic Chamber. The test instrumentation included a spinning mode probe to measure spinning mode content downstream of the treatment, radial probe traverses at four planes to separate forward- and backward-traveling modes, and a far-field traverse. All data acquisition and reduction were automated using the NASA-Langley ANRL computer facilities.

Based on the measured source mode data, analytical suppression predictions were made for comparison with experiment. Although experimental difficulties made interpretation of the theoretical/experimental correlation difficult in certain cases, sufficient data were obtained to confirm the validity of the prediction procedure.

Under the design frequency conditions of this study, it was found that multiple-treatment-element effects offered no appreciable suppression benefit, but boundary layer effects provided a phasing effect between the treatment section and upstream hard-wall length of duct which was very significant to overall optimum performance. At the design condition, an extraneous spinning mode content problem obscured the measured suppression. Based on the comparison of predicted and measured data, the panels are behaving as would be expected for panels of a given impedance at a given frequency.

*Kevlar: Registered trademark of E.I. du Pont de Nemours and Company

2.0 INTRODUCTION

The reduction of noise radiated from the inlet ducts of high bypass ratio turbofan engines is an important factor in allowing these engines to meet noise acceptability regulations for modern aircraft. At the present time, the most effective method for suppressing this inlet-radiated noise is lining the walls of the duct with absorptive acoustic treatment. The current state of the art of inlet treatment design is based on a combination of simplified duct propagation theory and empirical testing of scale models and full-scale engines. Further improvement in inlet treatment designs requires a more thorough investigation of the generation and propagation properties of acoustic wave patterns in the inlet duct, including the effects of mean flow with boundary layers.

This study was aimed at the investigation of the basic properties of spinning-mode wave propagation in a cylindrical duct under highly controlled laboratory conditions. The main objectives were to gain experience with, and evaluate (1) recent advances in experimental measurement of wave patterns and (2) the theoretical prediction of suppression for treatment panel designs. The testing utilized the NASA-Langley Research Center ANRL Anechoic Chamber. A treated cylindrical inlet duct was mounted, and the Spinning Mode Synthesizer Apparatus was used as a sound source. The theoretical prediction was based on a modal analysis procedure for multielement treatment panels developed originally by W. Zorumski (Reference 1).

The treatment panel designs were based on preliminary measurements of the modal patterns generated in the duct by the Spinning Mode Synthesizer. The treatment panels were constructed of the bulk absorber material Kevlar, which has properties that may make it potentially suitable for use in flight-worthy aircraft engines. A series of tests was conducted in the Anechoic Chamber to measure the performance of the treatment at design and off-design conditions. The measured suppression values were then compared to analytical predictions.

The choice of Kevlar bulk absorber as a treatment panel construction material was made on the basis of its ability to provide reliably predictable impedance components in the acoustic and flow environment of the inlet duct. Although bulk absorber treatment designs are known to possess suppression performance advantages over conventional single-degree-of-freedom resonator designs when the suppression bandwidths in the presence of wide bandwidth (broadband) noise are considered, the conditions of this study are not sufficiently broad to adequately illustrate this comparative behavior.

Use of trade names or names of manufacturers in this report does not constitute an official endorsement of such products or manufacturers, either expressed or implied, by the National Aeronautics and Space Administration.

3.0 ANALYTICAL PREDICTION PROGRAM

3.1 CYLINDRICAL DUCT PROPAGATION ANALYSIS

A prediction program for the analysis of wave propagation in cylindrical ducts of infinite length has been developed by W. Zorumski (Reference 1) of NASA-Langley Research Center. The basis for the prediction procedure is the analysis of the wave motion in terms of component modes, in this case the characteristic modes of a cylindrical duct. The modal propagation theory was extended by Zorumski to allow for multiple axial treatment sections, reflections at duct interfaces, and the presence of uniform mean flow. Input to the program consists of duct geometry, mean flow rate, treatment wall impedances, and the modal characteristics of the noise generation mechanism at the given source plane.

In each duct section with a different wall impedance, the program must determine the sequence of duct mode eigenvalues and eigenfunctions which apply to the given boundary conditions. These eigenfunctions are used in modal expansions to fit the required acoustic pressure patterns at treatment section interfaces. The accurate and foolproof determination of these eigenvalues is probably the most critical point of the entire calculation; most errors or failures of the prediction method can be traced to eigenvalue problems.

As part of this study, two major modifications were made to the Zorumski prediction program. First, a more reliable eigenvalue routine was developed primarily to avoid the double eignevalue problem, i.e., to prevent finding the same eigenvalue twice. This development is described in detail in Section 3.2. Second, the eigenvalue routine was extended to include the effects of thin, mean-flow, boundary layers at the duct walls. This procedure is based on an analysis developed by Nayfeh (Reference 2) and is described in Section 3.3.

3.2 CYLINDRICAL DUCT EIGENVALUE SEARCH ROUTINE

The modal analysis technique of duct acoustic propagation prediction is based on the expansion of spatial acoustic pressure patterns in the series of duct eigenfunctions. These eigenfunctions arise from the solution of the wave equation for the duct geometry involved and must satisfy given boundary conditions at the surfaces of the duct. In the case of the circular duct (no centerbody) the eigenfunctions take the form of Bessel functions of the first kind and the eigenvalues appear in the argument of the Bessel function.

The boundary conditions are obtained by matching the ratio of the acoustic pressure and the normal component of acoustic velocity for the wave solution at the wall to the acoustic impedance (or admittance) of the wall surface. The boundary condition equation obtained in this way contains the eigenvalue as an unknown parameter. Finding the eigenvalues which satisfy the equation is necessary to obtain the complete sequence of eigenfunctions.

In the case of the cylindrical duct with uniform mean flow, the boundary condition equation takes the form:

$$\beta_{kB} = \frac{i}{(1-M\Omega)^n} \left[\gamma \frac{J_{m+1}(\gamma)}{J_m(\gamma)} - m \right] \qquad (3.2\text{-}1)$$

where

β = normalized wall admittance

k = wavenumber ($2\pi f/c$)

f = frequency

c = speed of sound

B = duct radius

i = $\sqrt{-1}$

M = mean flow Mach number

n = boundary condition exponent (n=1 for continuity of particle displacement, n=2 for continuity of particle velocity)

γ = duct eigenvalue

J_m = m^{th} order Bessel Function of the first kind

m = spinning mode order

and

$$\Omega = \frac{\kappa}{k} = \frac{1}{k} \frac{-M \pm \sqrt{1 - (1-M^2)\left(\frac{\gamma}{kB}\right)^2}}{1-M^2} \qquad (3.2\text{-}2)$$

is the axial propagation constant. Equation 3.2-1 is a complex, transcendental equation for the sequence of roots, γ_j, and must be solved by numerical techniques.

For a modal analysis prediction program to be reliable in operation, it is essential that the eigenvalue search routine which extracts the roots of Equation 3.2-1 be as nearly foolproof as possible. The eigenvalues must be found in the correct order and found only once. Finding the same eigenvalue twice, the "double eigenvalue" problem, causes havoc with subsequent integrations of products of eigenfunctions which are performed in the modal analysis procedure.

A convenient method for graphically representing the boundary condition equation for the relationship between the wall admittance and the eigenvalue

is to plot it as a complex map in the eigenvalue plane. Figure 1 is an example of this mapping for the m = 0 spinning mode at Mach 0.0. In the figure, lines of constant magnitude of the admittance parameter βkB are plotted as solid lines, and lines of constant phase are plotted as dashed lines. Modal regions are separated by branch cuts of the complex map which are chosen to be lines of constant magnitude of βkB. These lines run through the branch points of the complex map, as indicated in Figure 1.

For a given value of βkB, one eigenvalue will be obtained in each of the modal regions separated by the branch cuts. If a Newton-Raphson type iteration scheme is chosen to extract the roots of the equation, it is necessary to supply initial guesses which, hopefully, will lead to convergence to the correct final values. In terms of the modal maps, it is necessary to choose initial values such that the iteration path from initial to final value never crosses a branch cut into the region of a different mode.

The easiest initial values to find are the hard-wall roots which occur along the real-γ axis. These guarantee that each initial value will start in a different modal region, but, if the desired root is too far from the hard-wall root, there is no guarantee that the iteration path will not cross a branch cut.

Eigenvalue problems of this kind were treated in considerable detail for the rectangular duct case in Reference 3. In Reference 3, the modal regions of the rectangular duct modal map were divided into subregions, each with its own initial value. A preprocessing routine determines the initial values based on the value of βkB. The subregions are small enough that the integration path within the subregion is maintained, guaranteeing that it will not cross a branch cut.

For the Mach 0.0 case, the modal maps can be normalized for frequency and duct height so that, by plotting the admittance parameter βkB, the map will apply to all values of kB. In the presence of mean flow, this is no longer possible (see Equation 3.2-1); therefore, the map will be different for each value of Mach number or kB. The curves of constant βkB magnitude and phase are distorted continuously in the eigenvalue plane as Mach number varies, holding kB constant. To find the eigenvalues in the presence of uniform mean flow, it is necessary to find the Mach 0.0 eigenvalues and then use them as initial values in a stepwise iteration procedure in which the Mach number is increased from 0.0 to its final value. At Mach 0.0, the eigenvalues for forward- and backward-traveling modes are identical, but they assume different values in the presence of mean flow. This necessitates separate iterations for forward and backward eigenvalues with flow. Convergence is guaranteed by taking sufficiently small Mach number steps.

The modifications to the Newton-Raphson iteration procedure to solve the eigenvalue equation have made the modal analysis prediction program extremely reliable in operation. The techniques were applied to the cylindrical duct prediction program eigenvalue equation as part of this study. An added difficulty in the cylindrical duct case, compared to the rectangular, was that

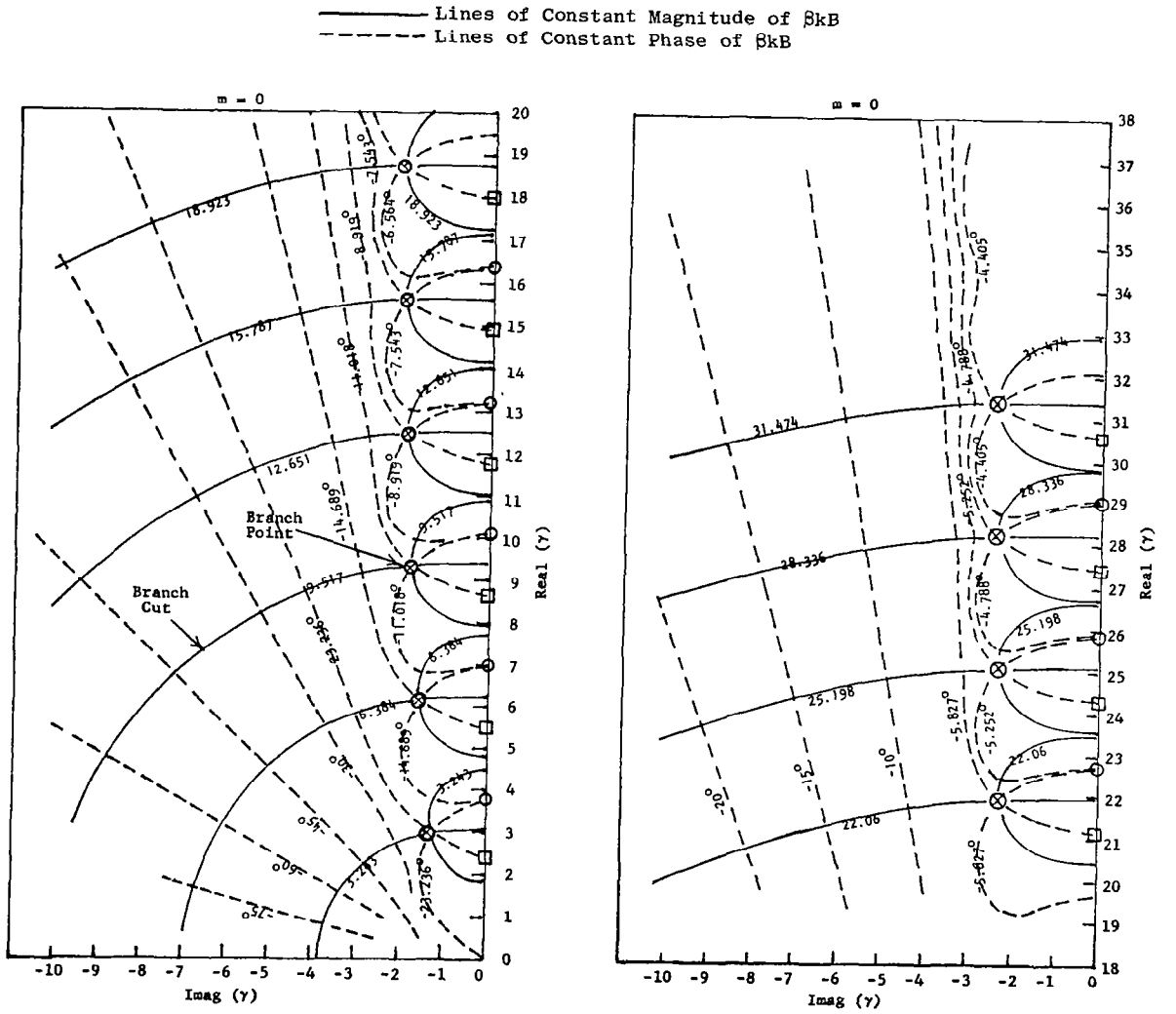

Figure 1. Contour Map of Admittance-Eigenvalue Relation for m = 0 Spinning Mode.

Mach 0.0 modal maps were required for every different spinning-mode order of interest, as opposed to only one map in the rectangular duct case.

An automated, computer-plotting routine was developed to produce the spinning mode maps for all spinning mode orders from m = 0 to m = 50. An example of a modal map produced by the computer for the m = 3 mode is shown in Figure 2. An example of the subpartitioning scheme is shown in Figure 3 for the m = 30 mode; the initial values in each region are marked with an X. In order to standardize the choice of subregion boundaries, curves of βkB magnitude and phase which pass through the branch point were used, as shown. A separate iteration scheme was written to search out the locations and βkB values at the branch points with high accuracy. To find initial eigenvalues in the region to the left of the subpartition regions, an exponential approximation based on the circular shape of the curves was used.

Rather than storing each of the initial values in the preprocessing routine along with the βkB criteria to find each value separately, it was found that the subregions could be grouped into classes such that the initial values formed relatively smooth functions of spinning mode order and radial mode order. Polynomial curve-fit routines were then developed to determine functions which calculated the initial values depending on the particular class of subregion in which they are found. The preprocessor will supply initial values for the first 11 radial modes for spinning mode orders from m = 0 to m = 50.

The initial values are then iterated to the correct Mach 0.0 eigenvalues using a Newton-Raphson iteration technique which finds the roots of the function

$$F(\gamma) = \beta kB - i\left[\gamma \frac{J_m(\gamma)}{J_{m+1}(\gamma)} - m\right] \qquad (3.2\text{-}3)$$

The iteration uses a second-order form of the Newton-Raphson formula (Bailey's Method), such that

$$\gamma_{j+1} = \gamma_j - \frac{FF'}{(F')^2 - \frac{1}{2}FF''} \qquad (3.2\text{-}4)$$

where j is the iteration number, and the primes denote derivatives with respect to γ.

The converged Mach 0.0 eigenvalues are then used as initial values for an equivalent Newton-Raphson iteration of the function

$$F(\gamma) = \beta kB(1-M\Omega)^n - i\left[\gamma \frac{J_m(\gamma)}{J_{m+1}(\gamma)} + m\right] \qquad (3.2\text{-}5)$$

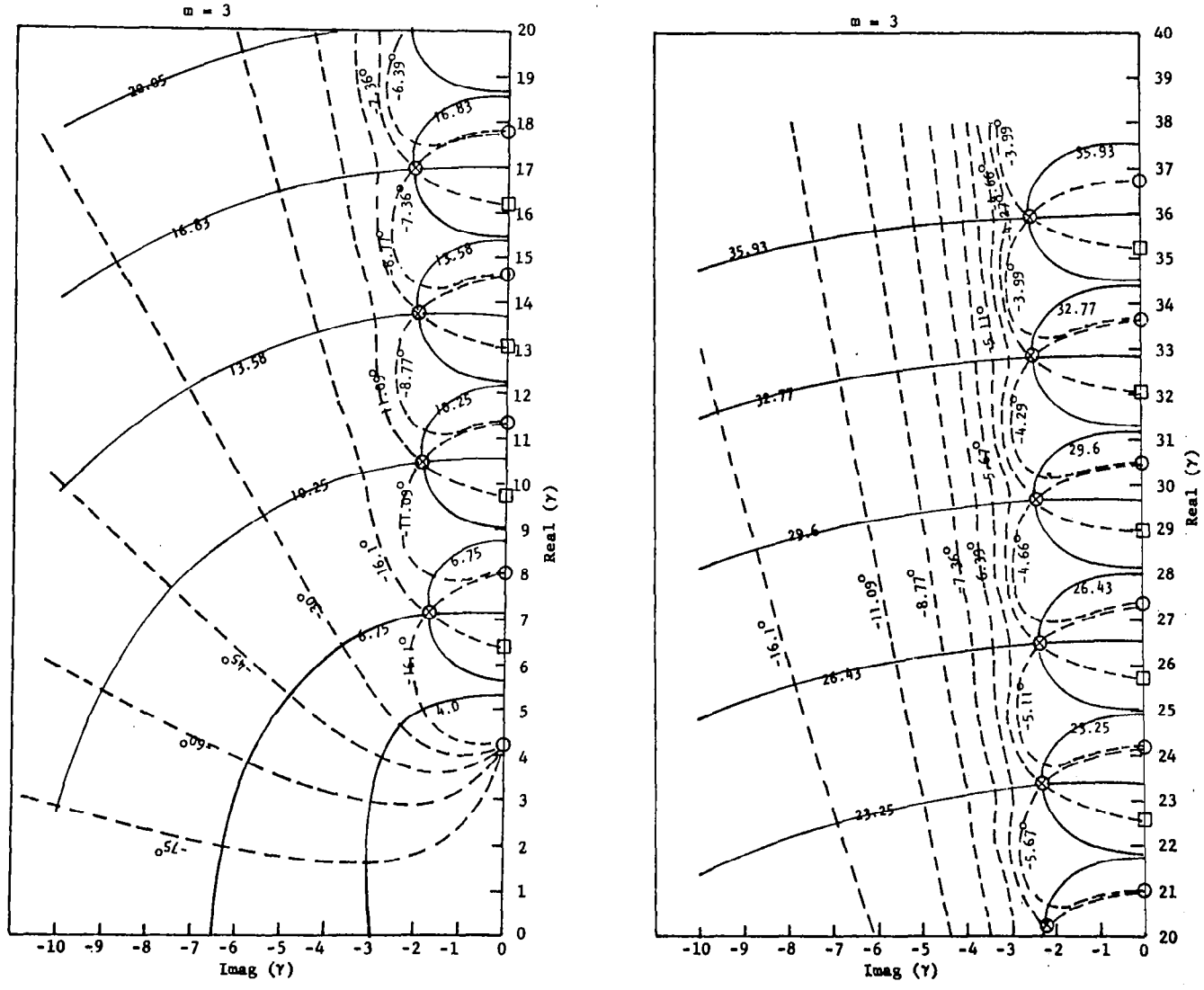

Figure 2. Computer-Generated Contour Plot of Admittance-Eigenvalue Relation for m = 3 Spinning Mode.

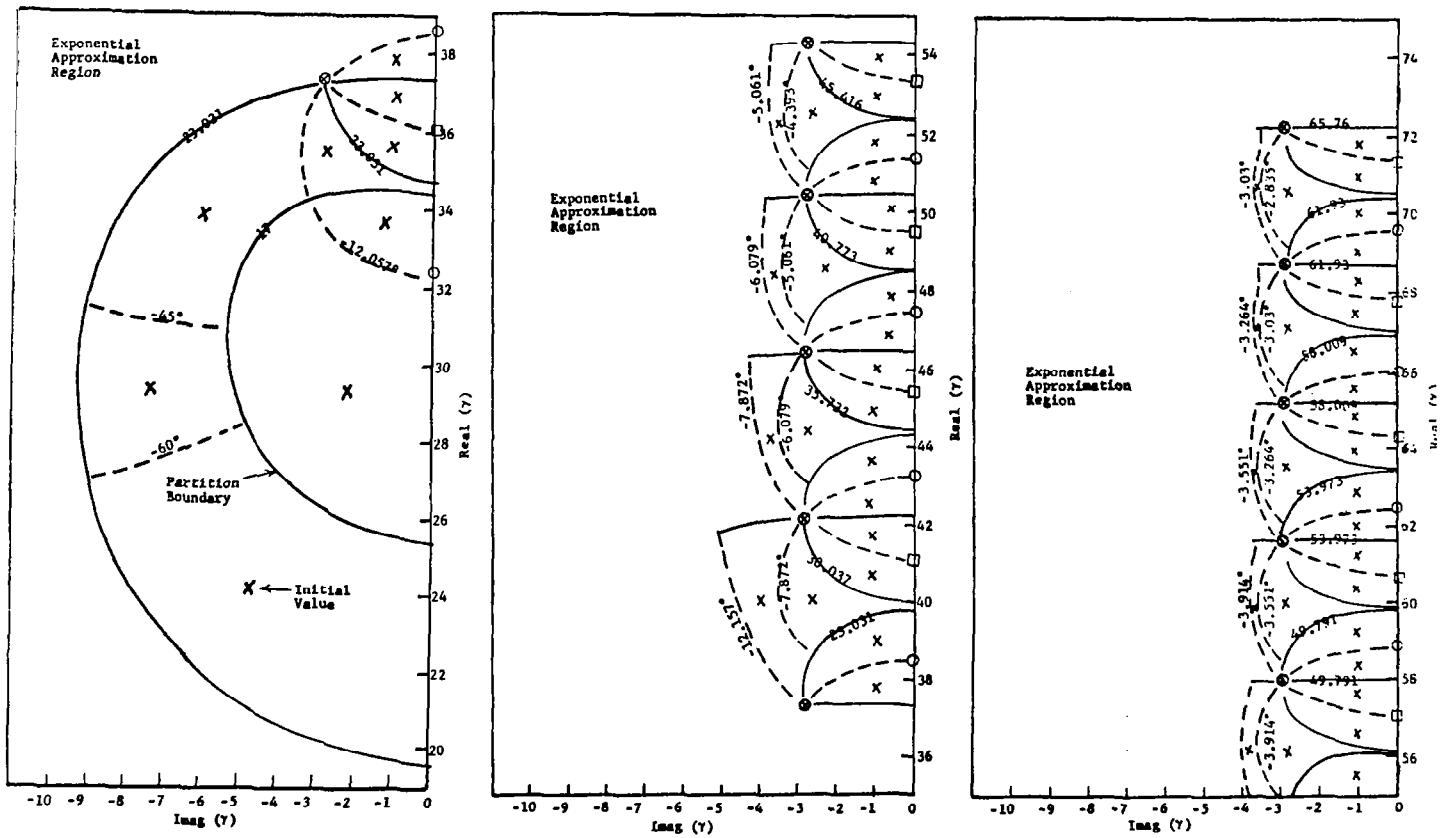

Figure 3. Initial Value Partitioning Scheme for m = 30 Spinning Mode Admittance-Eigenvalue Mapping.

which is the uniform mean flow form. In practice, 10 steps in the Mach number are usually sufficient to guarantee convergence.

The eigenvalues with uniform flow are then used as initial values to find the eigenvalues in the presence of thin boundary layers. The development of this modification to the eigenvalue program is considered in the next section.

3.3 EIGENVALUES IN THE PRESENCE OF BOUNDARY LAYERS

Acoustic wave propagation in ducts with mean flow can be influenced by the presence of shear layers near the wall boundaries. From a geometric acoustics point of view, the shear layers act to refract the acoustic wavefronts either toward or away from the wall, depending on whether the wave is traveling in the same direction or the opposite direction as the mean flow. A basic assumption for this analysis will be that the boundary layers can be considered thin, from an acoustical standpoint, so that the predominant part of the acoustic energy flux takes place in the uniform flow region of the cross section, and energy flux variations in the boundary layer regions can be neglected. In this sense, the boundary layers can be thought of as providing an effective impedance condition at the wall, modifying the impedance of the treatment panel for each mode.

By assuming that the flow in the boundary layer remains parallel to the duct walls, the differential equation for the radial variation of acoustic pressure in the presence of a shear layer can be put in the form:

$$\frac{d^2p}{dr^2} + \frac{1}{r}\frac{dp}{dr} + \frac{2\Omega}{1 - M\Omega}\frac{dM}{dr}\frac{dp}{dr} + \left(\alpha^2 - \frac{m^2}{r^2}\right) p = 0 \qquad (3.3\text{-}1)$$

where

p = acoustic pressure

r = duct radial variable

Ω = normalized axial propagation constant (see Equation 3.2-2)

M = Mean flow Mach number (function of r)

α = eigenvalue ($\gamma = \alpha B$)

m = spinning mode order

Note that when the derivative of Mach number with respect to radius is zero, Equation 3.3-1 reduces to the standard Bessel equation. The boundary condition expressed in Equation 3.2-1 still applies at the wall, where M takes on the value of the Mach number at the wall.

The rigorous solution to Equation 3.3-1 with boundary condition 3.2-1 for arbitrary wall admittance requires the determination of eigenfunctions which satisfy the differential equation, both in the uniform- and in the nonuniform-flow regions of the duct, and eigenvalues which match the wall admittance condition. The eigenfunctions, if it were possible to find them, would be different for every different shape of the flow profile. The method of solution adopted here is approximate in that the eigenfunctions are chosen to be of the same form as in the uniform-flow case, with eigenvalues modified by the effects of the boundary layer.

Thus, in the uniform flow region, the acoustic pressure is given by:

$$p(r) = J_m\left(\gamma \frac{r}{B}\right) \qquad (3.3\text{-}2)$$

and the derivative of the pressure (proportional to the acoustic velocity) is:

$$q(r) = \frac{\gamma}{B}\left[- J_{m+1}\left(\gamma \frac{r}{B}\right) + \frac{m}{\gamma \frac{r}{B}} J_m\left(\gamma \frac{r}{B}\right)\right] \qquad (3.3\text{-}3)$$

This solution applies up to the edge of the boundary layer. If we were to choose a value of γ, Equations 3.3-2 and 3.3-3 could be used to determine p and q at the edge of the boundary layer, where

$$r = B - \delta \qquad (3.3\text{-}4)$$

if δ is the boundary layer thickness. Using Equation 3.3-1, a forward integration procedure can be used to numerically integrate p and q through the boundary layer starting with the initial values at the edge. At the wall, this solution will give an admittance equal to

$$\beta_{kB} = -i \frac{B\, q(B)}{(1-M\Omega)^n\, p(B)} \qquad (3.3\text{-}5)$$

This may or may not be equal to the desired wall admittance, depending on the value of γ chosen for the uniform-flow solution.

By varying γ, it is possible to establish an iteration procedure to achieve any desired admittance at the wall. This technique forms the basis for calculating the eigenvalues in the presence of the boundary layer. An initial guess at the eigenvalue is determined by using the uniform-flow (no boundary layer) eigenvalues as found by methods outlined in the previous section. A Runge-Kutta four-point, numerical-integration scheme was developed to integrate the pressure and its derivative through the boundary layer. By varying γ slightly and integrating again, derivatives of wall admittance with respect to γ can be calculated, allowing a Newton-Raphson iteration scheme to be used to converge on the value of γ which provides any arbitrary wall admittance.

Although this procedure could be used with an arbitrary boundary layer flow profile, a particular profile was chosen based on the results of a study by Nayfeh, Kaiser, and Shaker (Reference 2). These authors propose that a linear boundary layer profile with nonzero flow velocity at the wall may be quite suitable for acoustic purposes. This profile, shown in Figure 4, is based on the scaling factors of shape (ratio of displacement thickness to momentum thickness) and displacement thickness. These factors were found to correlate modal attenuation rates for a variety of mean profile shapes. Selecting a linear profile which has the same shape factor as a turbulent, one-seventh-power law profile, the ratio of wall (slip flow) Mach number to mean flow Mach number, according to Reference 2, is:

$$\frac{M_w}{M} = \frac{2}{3} \qquad (3.3\text{-}6)$$

and the boundary layer thickness is six times the displacement thickness.

In the above derivation, it is important to note that the eigenvalue and axial-propagation constant for each mode are held constant during the numerical integration through the boundary layer, even though the axial propagation constant is ostensibly a function of Mach number (see Equation 3.2-2). This is a consequence of the thin boundary layer assumption and assures that the mode propagates through a section of uniformly treated duct with unchanging mode shape and unique axial wavelength and attenuation rate. The condition of continuity of particle velocity is used at the wall.

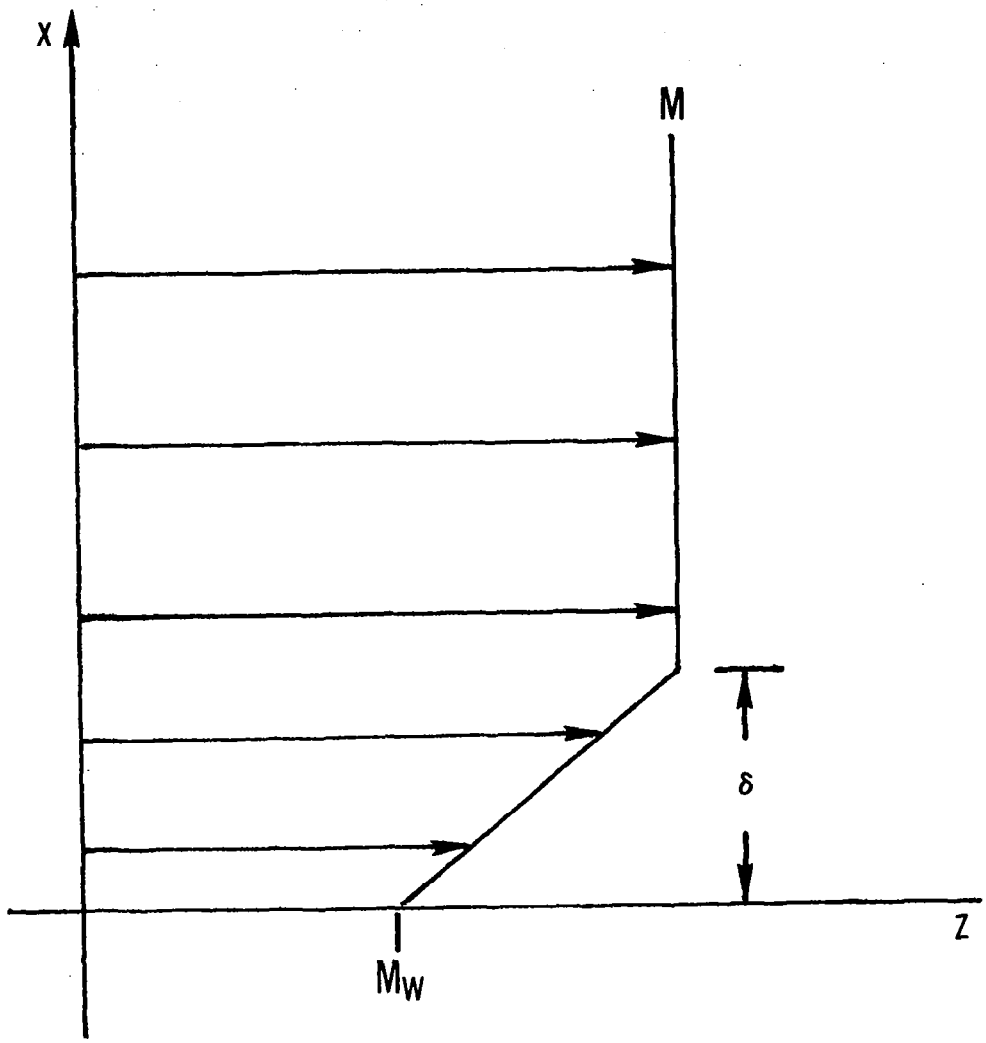

Figure 4. Equivalent Boundary Layer Profile used for Analysis, Based on Reference 2.

4.0 OPTIMIZED TREATMENT DESIGN

The principal objective of this program was the analytical design and experimental test of optimized bulk absorber treatment configurations for an inlet duct. The analytical design was accomplished using the cylindrical duct prediction program with the modified eigenvalue routine using input parameters determined by preliminary measurements in the NASA-Langley Research Center ANRL Anechoic Chamber. The design optimization procedure considered multielement, or segmented, acoustic liners with a maximum overall treatment length equal to one diameter 30.5 cm (12 inches). The bulk absorber designs make use of the aramid fiber material Kevlar manufactured by Du Pont Chemical Corporation. This material has been identified to have properties making it potentially acceptable for use in flight-worthy aircraft engines.

This section presents the choice of design parameters, the method and results of the design impedance optimization, and the mechanical design of the panels.

4.1 DETERMINATION OF DESIGN PARAMETERS

In order to begin the design optimization process, it was necessary to choose a frequency, spinning mode order, and mean-flow Mach number for input to the prediction program. Since the designs were to be tested in the inlet flow duct facility mounted in the NASA-Langley Anechoic Chamber, the parameters chosen were required to be compatible with the operation of this apparatus. A series of preliminary tests was run in the duct facility using the Spinning Mode Synthesizer as a sound source to determine these design and test conditions.

A major advantage of the use of the Spinning Mode Synthesizer sound source (which will be described in more detail in the Test Program section) is its ability to generate a relatively pure spinning mode, i.e., a circumferential spinning mode pattern which is dominated by a single spinning-mode order, spinning in one direction. This condition is important for subsequent in-duct tests to measure the performance of the treatment designs, because the in-duct measurement method (as described later) is based on the assumption that only a pure spinning mode pattern is present. It was hoped that testing under these controlled conditions would allow a very accurate correlation between theoretical prediction and experimental measurement.

A complete list of the design parameters is assembled in Figure 5.

4.2 TREATMENT OPTIMIZATION

The original intent of the design optimization procedure was to determine single-element, two-element, and three-element treatment configurations, each with the same ratio of overall treated length to duct diameter (L/D), where the treatment panels are arranged in the conventional sense of multiphasing,

Spinning Mode Order: $m = 3$

Frequency: $f = 2740$

η-Value ($\eta = D/\lambda$): $\eta_D = 2.4$

Mean Flow Mach Number: $M = 0.2$

Boundary Layer Profile:

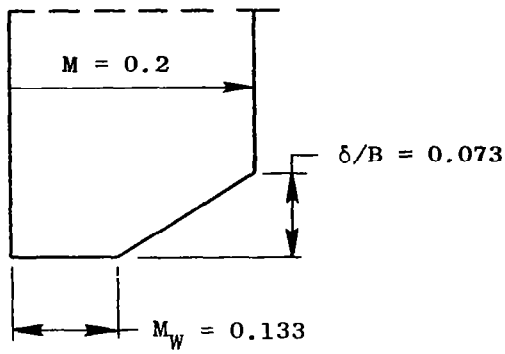

Radial Mode Content: Only Lowest Order Radial Mode Given Weighting

Figure 5. Optimized Treatment Design Parameters.

as shown in Figure 6. Experience at General Electric (Reference 4) has shown that the effects of multiphasing are quite sensitive to the value of the ratio of duct diameter to wavelength η ($\eta = D/\lambda$) at which the design is being made. At η values for which only one radial mode is cut-on for a given spinning mode order, multiphasing effects are likely to be small, but even the single-phase liner will give high suppression. The design conditions for this study, which were determined by the need to choose a frequency at which only one radial mode was allowed to propagate, fall into the low η-value category.

The procedure for determining the optimum wall impedance for the single-phase treatment configuration of a given length is straightforward. Overall suppression is plotted in the impedance plane as impedance is varied parametrically, allowing the plotting of contours of constant attenuation which peak at the optimum value.

The suppression of a single-element optimized liner was found to be affected by three different suppression mechanisms in the presence of a boundary layer. First, there is the ordinary dissipation in the liner due to absorption. Second, there is an appreciable energy reflection at the upstream interface of the liner and the hard-wall duct, denoted by Plane 3 in Figure 7. The reflection at Plane 2 was found to be negligible in all cases. Third, there is an attenuation of energy in the hard-wall section of the duct upstream of the treatment due to the presence of the boundary layer.

While Mechanisms 1 and 2 are present for uniform flow or no flow, this third effect occurs only because of the presence of the boundary layer. The boundary layer provides an "effective" impedance in the hard-wall section. The optimization process leads to a treatment impedance which affects the propagation in the lined section in such a way that the modal redistribution of radial modes into the hard-wall section between Planes 3 and 4 gives a pressure pattern which can be effectively attenuated in this hard-wall section. This is entirely different from the suppression which would be expected in the no-mean-flow or uniform-mean-flow cases, where the upstream hard-wall attenuation would not occur and more suppression would take place over the treatment, which would have a different impedance value.

The overall optimum suppression for the single-phase liners as a function of L/D is plotted in Figure 8. This interpretation is obtained from examination of the forward and backward energy flux calculated in the modal analysis prediction program. In making these calculations, the overall distance between measurement Planes 1 and 4 is held constant, and the location of the leading edge of the treatment at Plane 2 is held constant. As the length of the treatment is decreased, the length of upstream hard-wall section between Planes 3 and 4 is correspondingly increased. Since the forward and backward modal energy flux is coupled in the presence of mean flow, the values are approximate, but they are sufficiently accurate to represent the process. The optimum impedance components for the single-phase liner are shown in Figure 9 both as a function of L/D and as a continuous curve in the impedance plane.

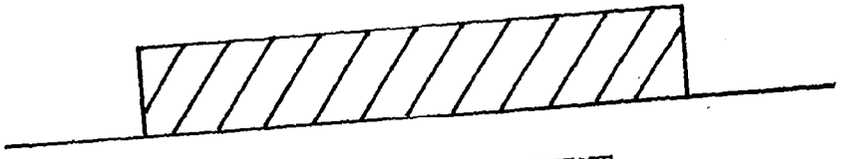

SINGLE-PHASE TREATMENT

TWO-PHASE TREATMENT

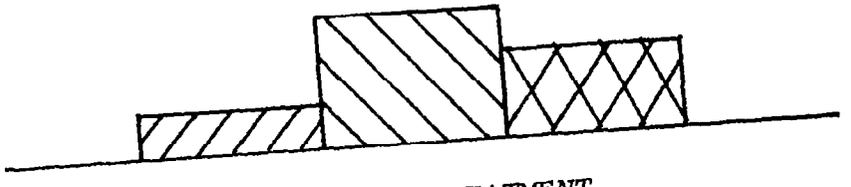

THREE-PHASE TREATMENT

Figure 6. Illustration of Single-Phase, Two-Phase, and Three-Phase Treatment Configurations.

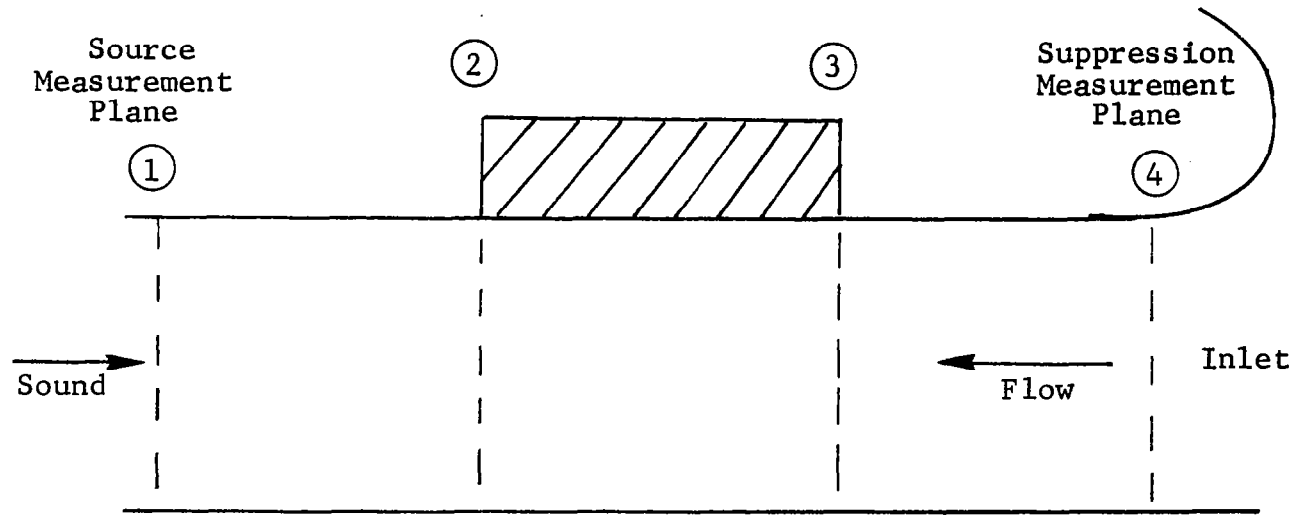

Figure 7. Single-Phase Treatment Diagram.

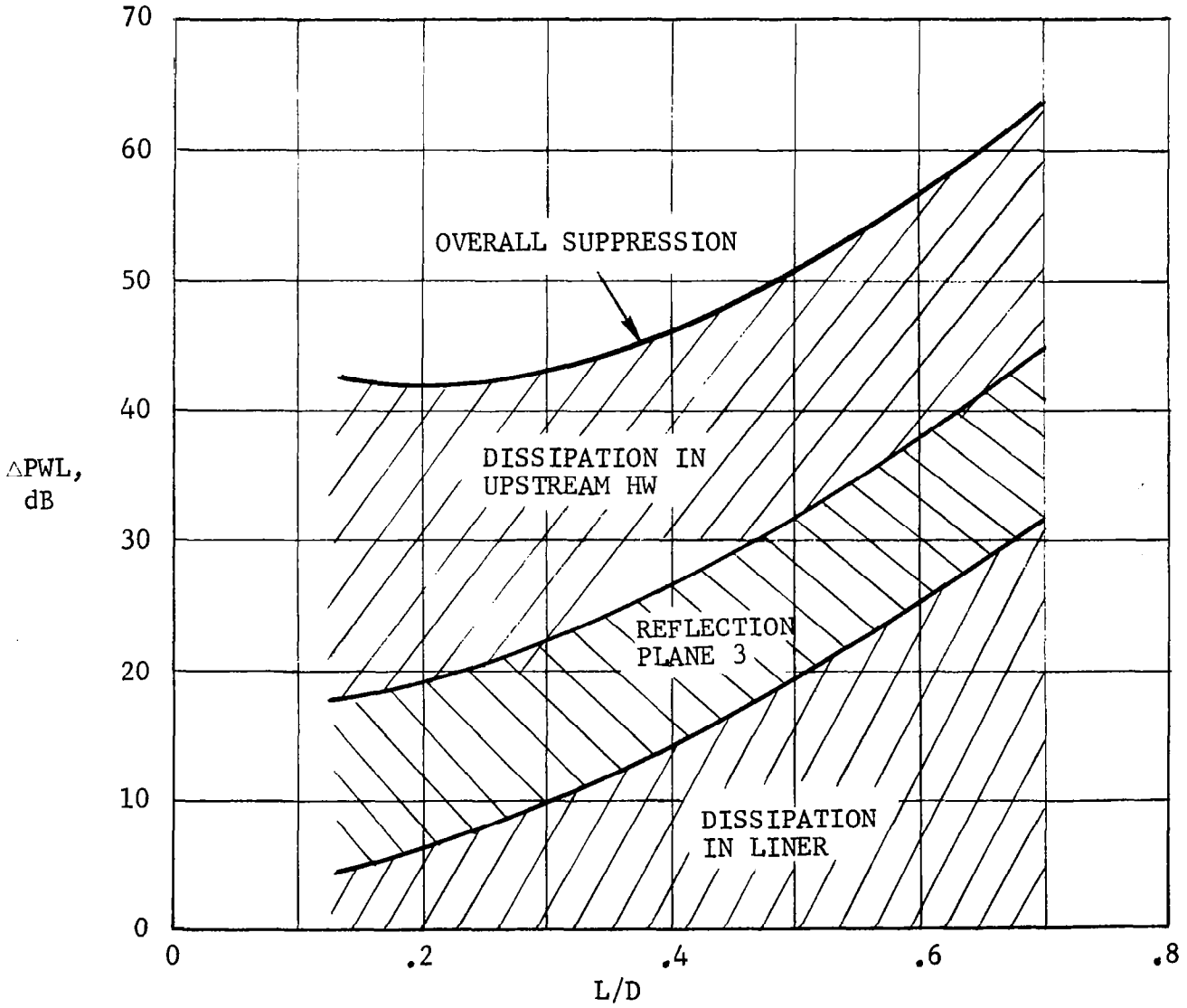

Figure 8. Suppression Effects for Single-Phase, Optimum Treatment Design Versus Treatment Length/Diameter Ratio.

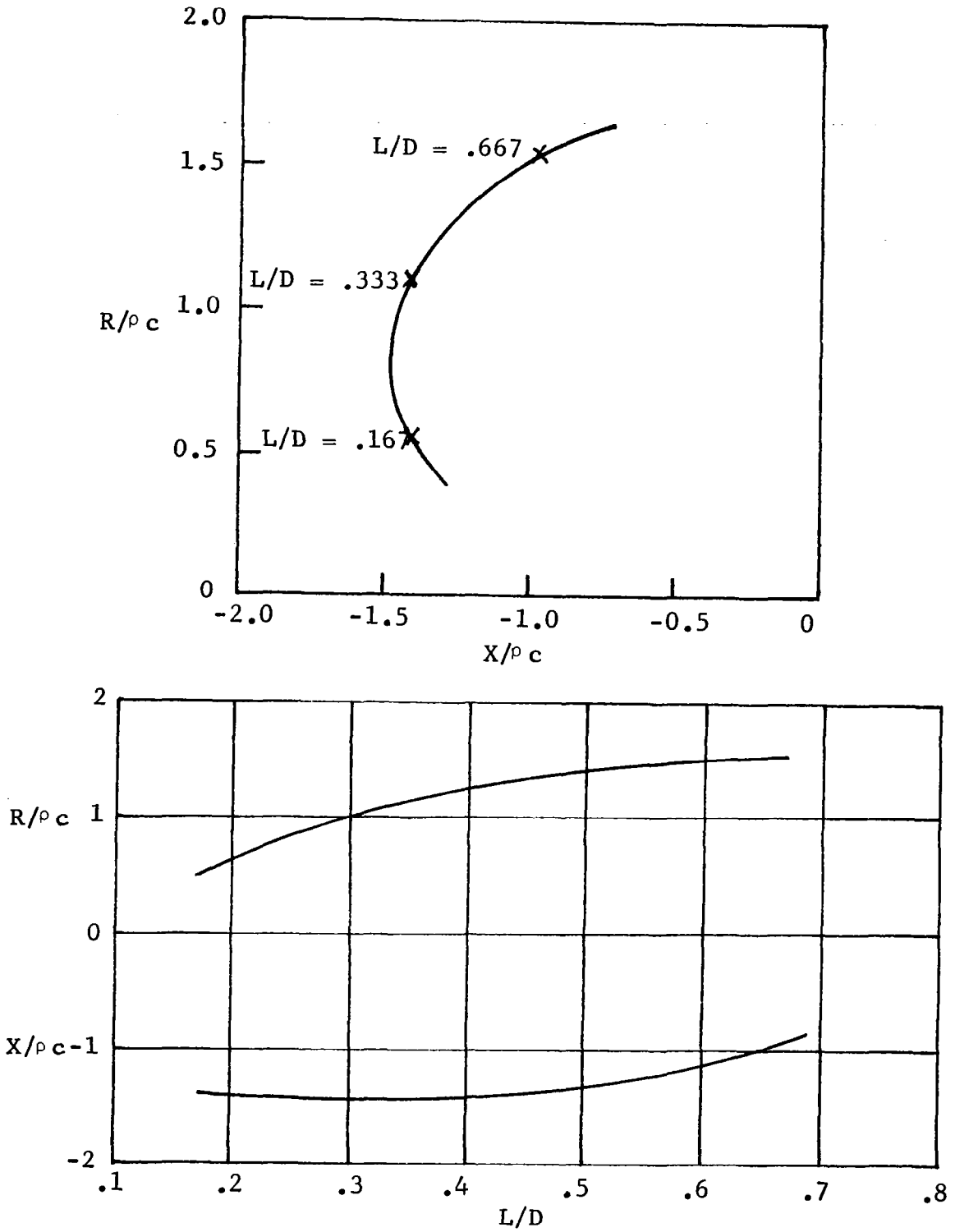

Figure 9. Optimum Single-Phase Liner Impedance Components as a Function of Treatment Length/Diameter Ratio.

The design optimization procedure for a multiphase liner is initiated with an optimized, single-phase liner of the same overall treatment length, divided axially into more than one section, after which each subsection is optimized individually in a sequential fashion. During the iterative procedure, the lengths of the individual segments are held constant. Starting with the 20.3-cm (8-inch) long, single-phase, optimum liner, this procedure was initiated by dividing the liner into two 10.2-cm (4-inch) lengths. By varying the impedance of either the upstream or the downstream segment, it was found that the overall suppression could not be increased more than a few tenths of a dB above that of the single-phase, optimum liner. This same procedure was attempted with a 5.1-cm (2-inch) downstream and 6.2-cm (6-inch) upstream split in segments, with similar results.

This result for multiphase optimization is a consequence of the low η-value for the m = 3 spinning mode at this frequency. Under the conditions of this study, the effects of conventional multiphasing provide no substantial benefits. It should be noted, however, that even the single-phase treatment configurations are acting as multiple-section suppressors between Planes 1 and 4, which are always kept at constant separation, when the effects of the hard-wall section between Planes 3 and 4 are considered. The boundary layer, therefore, provides an unconventional, or restricted, multiphasing effect in that the treated and hard-wall sections work in conjunction to increase suppression. This can also be considered to be an increase in the effective ratio of treated length to duct height for the inlet. Even higher suppressions could be obtained if the restriction of making the wall between Planes 3 and 4 a hard wall could be lifted, and arbitrary treatment inserted. Based on this result, no further attempt was made to search out conventional multiphase optimum design configurations.

An interesting observation from Figure 8 is that very little suppression is lost as the treated length is decreased below an L/D value of about 0.4; so that, for instance, a 5.1-cm (2.0-inch) liner (L/D = 0.167) gives nearly as much suppression at optimum as a 10.2-cm (4.0-inch) liner (L/D = 0.333). Based on this result, two of the treatment configurations to be built for test were chosen to be the 5.1 cm and 10.2 cm, single-phase optima. The nature of these two optimum conditions is shown in the contour plots of lines of constant suppression in the impedance plane, shown in Figures 10 and 11 for the 10.2-cm and 5.1-cm cases respectively. Note the sharpness of the suppression peaks in both cases, indicating a stringent design criteria.

Most of the suppression for the 5.1-cm optimum single-phase treatment configuration occurs in the hard-wall duct section upstream of the treatment. In order to take advantage of this hard-wall suppression effect, the question was raised as to what would happen if a second 5.1-cm optimum panel, separated by a hard-wall section from the first, were added to the duct. The results are shown plotted as a function of separation distance in Figure 12. At zero separation distance, the 10.2-cm panel with the 5.1-cm optimum impedance gives only 10-dB suppression, less than 25% of the 10.2-cm optimum value. As the two 5.1-cm panels increase in separation the overall suppression increases, but the separation must exceed 25.4 cm (10 inches) before the suppression level becomes greater than the solitary 5.1-cm optimum panel, due to coupling effects.

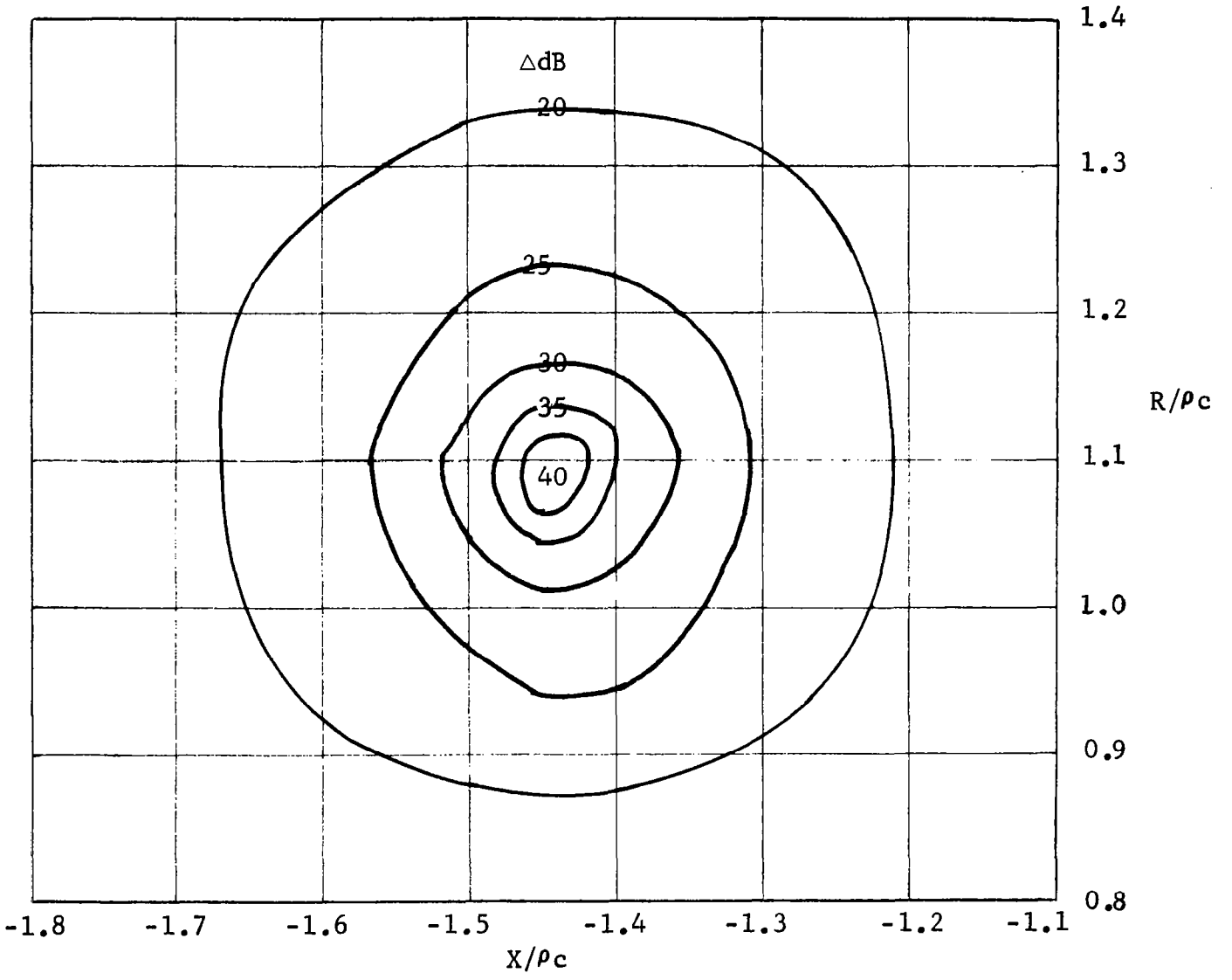

Figure 10. Suppression Contours in Impedance Plane for 10.2-cm (4-Inch) Long Treatment Panel.

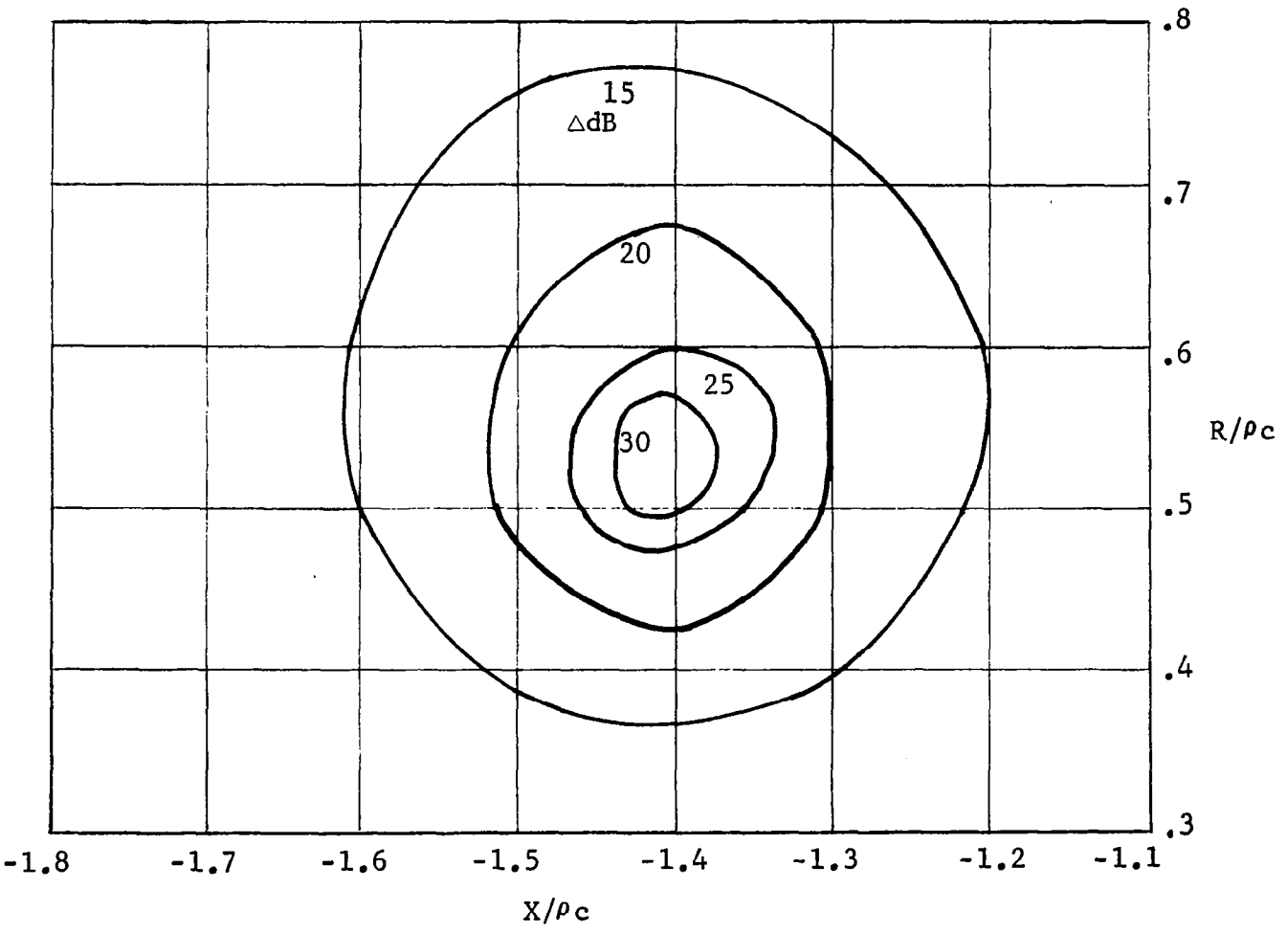

Figure 11. Suppression Contours in Impedance Plane for 5.1-cm (2-Inch) Long Treatment Panel.

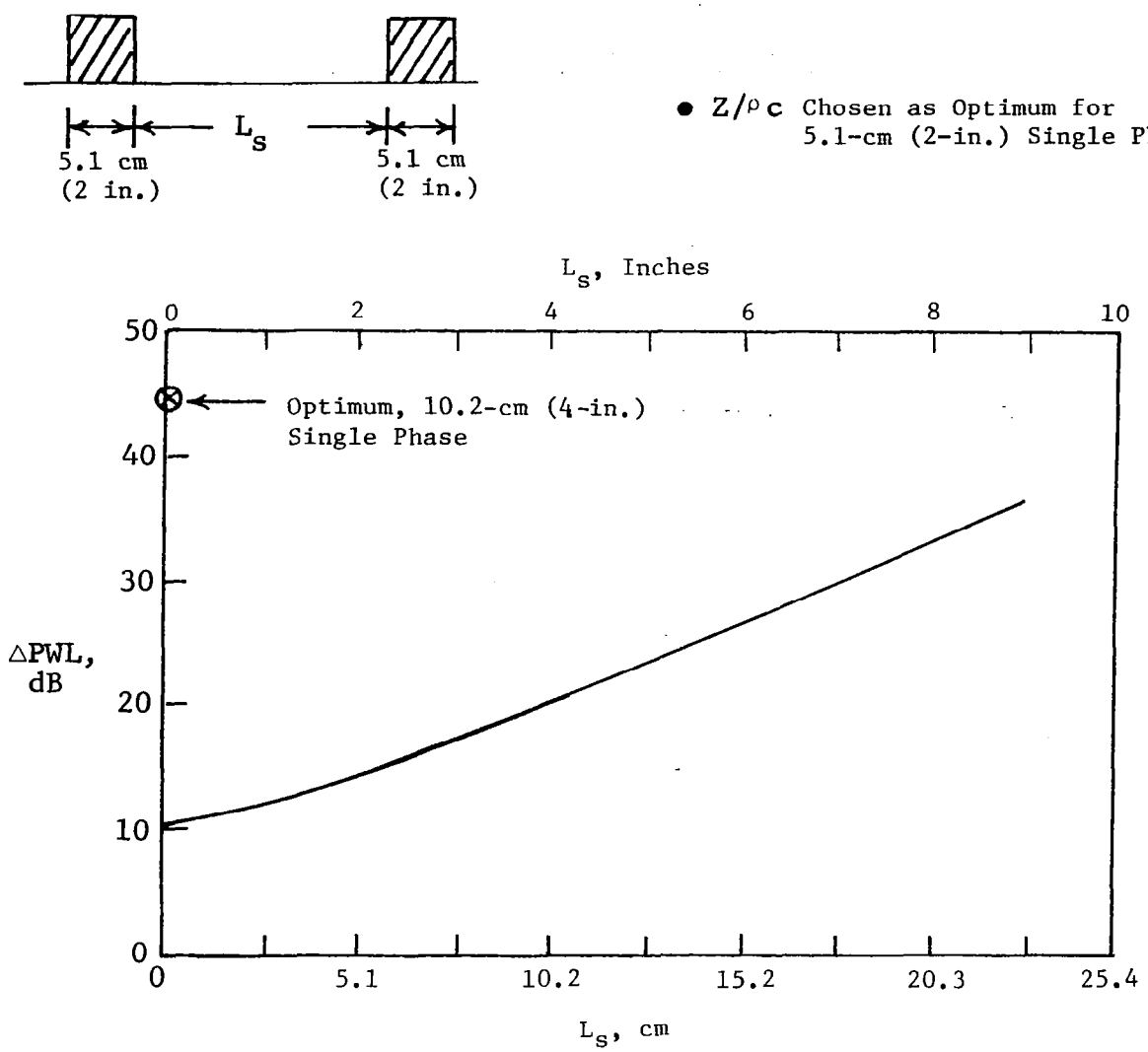

Figure 12. Suppression of Tandem, 5.1-cm (2-Inch), Single-Phase, Optimum Treatment Panels as Separation is Increased.

As a variation of this concept, in order to determine a third treatment configuration for test, an optimization study was conducted in which the downstream panel was maintained at the 5.1-cm, single-phase optimum impedance and a second 5.1-cm panel was located at 17.0-cm (7-inches) separation from the downstream panel, as shown in Figure 13. The impedance of the upstream section was varied parametrically to maximize suppression, and the results are shown in the contour map in Figure 14.

A summary of the three optimized treatment dsigns is shown in Figure 15.

4.3 TREATMENT PANEL DESIGN

The optimized treatment impedances from Figure 15 were translated into four different panel designs:

1. 10.2-cm (4-inch), Single-Phase, Kevlar
2. 10.2-cm (4-inch), Single-Phase, Single-Degree-of-Freedom (SDOF)
3. 5.1-cm (2-inch), Single-Phase, Kevlar
4. 5.1-cm (2-inch) + 5.1-cm (2-inch) (Two Segments), Kevlar

The Kevlar panel designs were accomplished using a conventional standing wave tube to measure impedance. It is assumed that the effects of mean flow and high sound pressure levels on the impedance of Kevlar panels are small, so that this measurement should be satisfactory for these panels. Two types of Kevlar material were available for the panel design. The first, denoted as the "fluffy" type, is a loosely woven material with a density of 93 kg/m^3 (0.58 lb/ft^3). The second, denoted as "dense" type, is a felt mat material of 200 kg/m^3 (1.25 lb/ft^3). The materials can be mixed in layers and compressed to obtain the desired impedance.

The Kevlar designs were accomplished by measurement trial and error using the standing-wave tube. The result of the 10.2-cm (4-inch) optimum design, with a target impedance of 1.10-1.45i, was two layers of "fluffy" Kevlar over two layers of "dense" Kevlar, compressed to a depth of 0.97 cm (0.38 inches). The panel is covered by 0.064-cm (0.025-inch) thick perforated plate, of 40.3% open area ratio, which functions only to contain the Kevlar. The nominal value of the measured impedance in this case was 1.0-1.4i. The 5.1-cm (2-inch) optimum was designed to a 1.02-cm (0.40-inch) depth with two layers of "fluffy" Kevlar. This gave a measured nominal impedance of 0.5-1.4i, compared with the target impedance of 0.525-1.40i. It was also covered by the same 40.3% porosity faceplate. Figure 16 shows the envelope of expected impedance values for these two panels, based on repeat measurement differences for the standing wave tube, plotted on top of the optimum suppression contours. Note that variations in calculated suppression of over 10 dB are possible due to impedance variation.

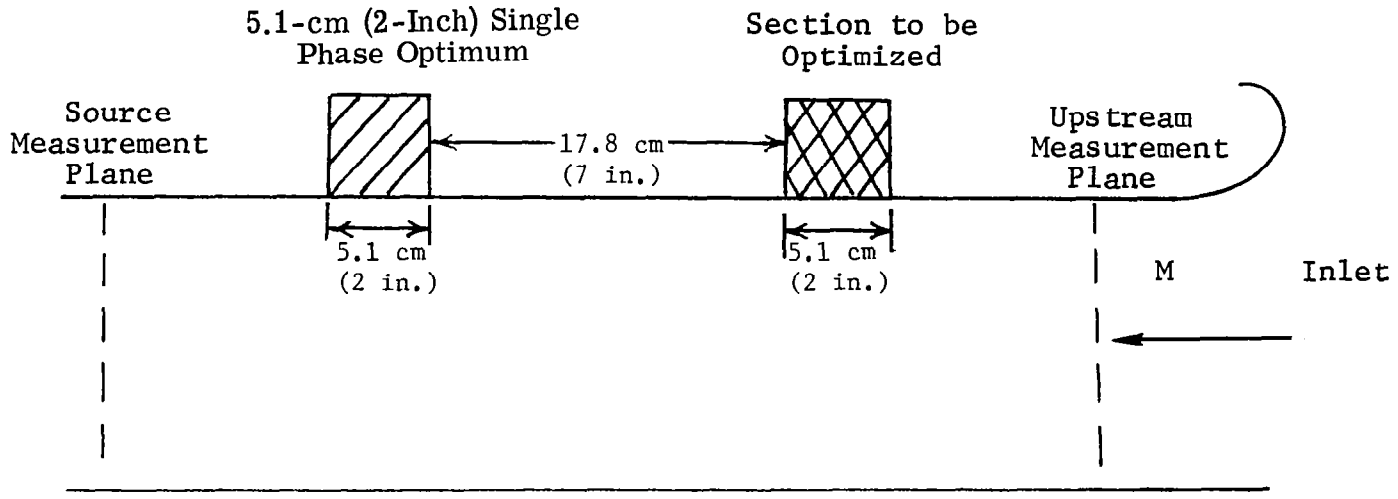

Figure 13. Separated Two-Panel Treatment Configuration.

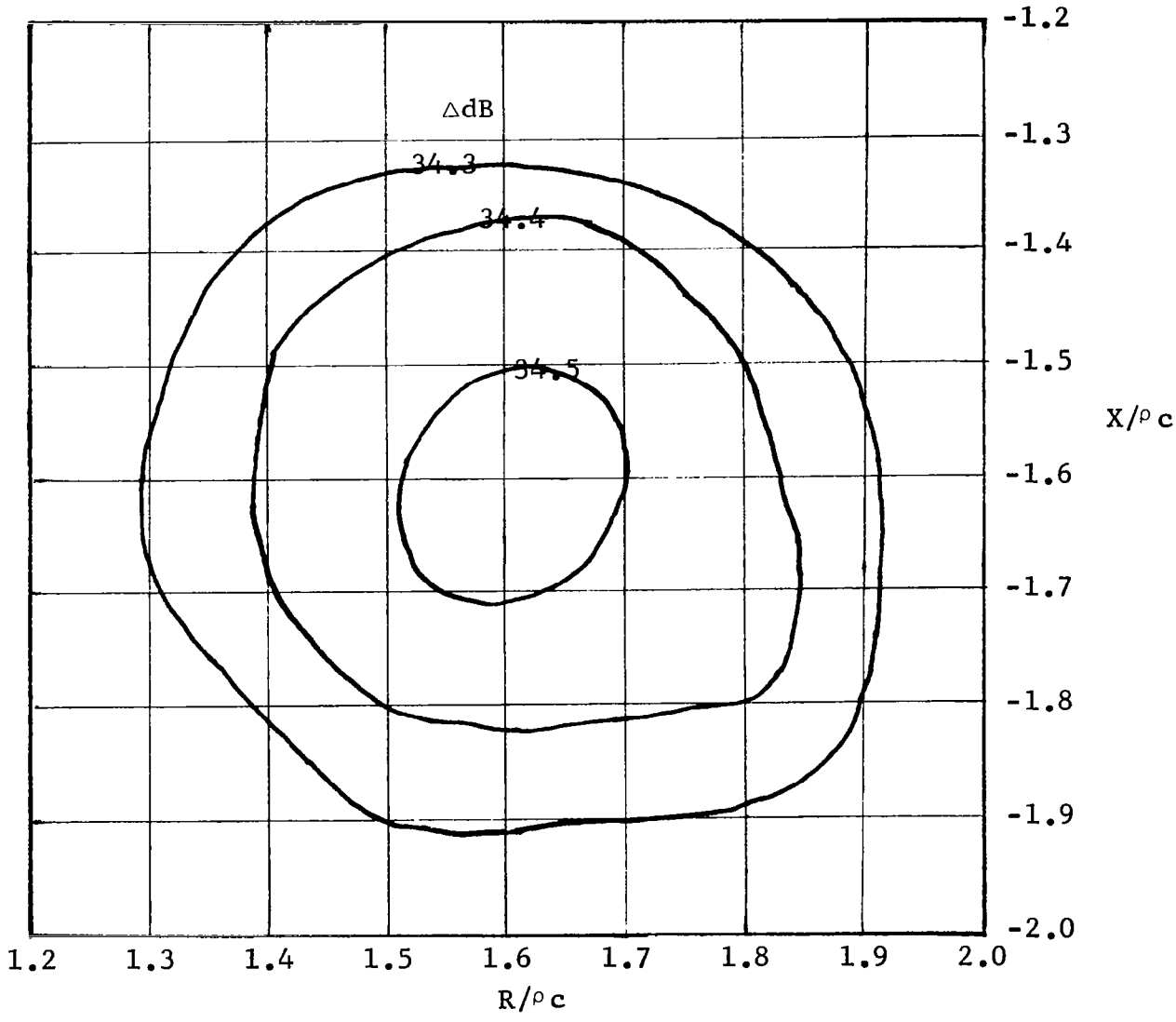

Figure 14. Suppression Contours for Separated, Two-Panel Configuration as a Function of Impedance of Upstream Panel, Holding Downstream Panel Constant.

1. 10.2 cm (4 in.) Single-Phase Optimum

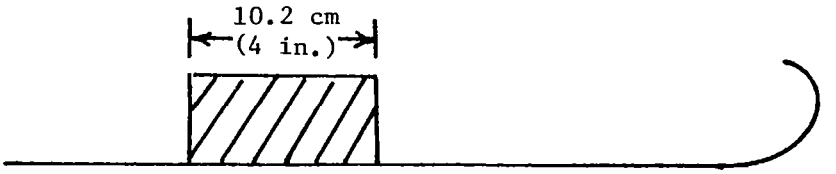

$Z/\rho c = 1.10-1.45i$ $\Delta PWL = 44.3$ dB

2. 5.1 (2 in.) Single-Phase Optimum

$Z/\rho c = .525-1.40i$ $\Delta PWL = 40.3$ dB

5.1 cm + 5.1 cm (2 in. + 2 in.) Separated

3. Two-Panel Optimum

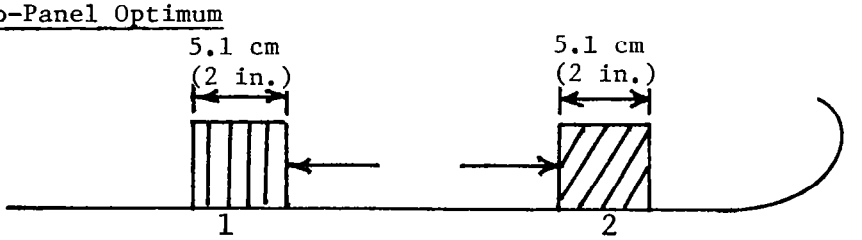

$Z_1/\rho c = .525-1.40i$

$Z_2/\rho c = 1.60-1.60i$

$\Delta PWL = 34.5$ dB

Figure 15. Optimized Treatment Design Configuration.

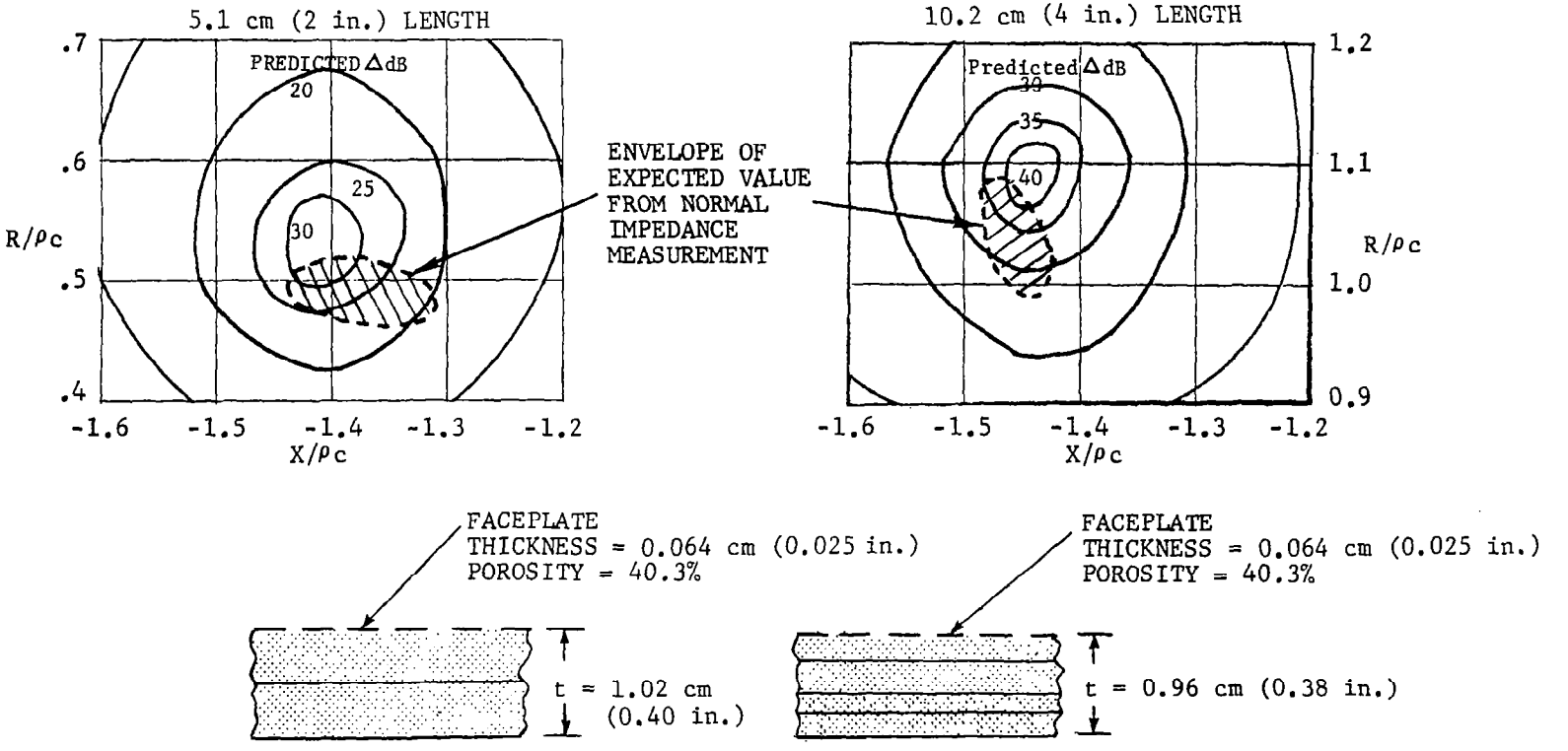

Figure 16. Variations in Suppression Due to Expected Variations in Impedance for Single-Phase Kevlar Optimum Impedance Values.

The construction of the upstream segment for the 5.1-cm + 5.1-cm optimum configuration utilizes four layers of dense Kevlar compressed into a 0.84-cm (0.33-inch) deep cavity, covered by the 40.3% porosity faceplate. It gave a nominal measured impedance of 1.6-1.6i, which is equivalent to the design goal. In all panels, axially oriented partitions were spaced circumferentially around the liners to provide barriers to circumferential wave propagation within the panel. It is assumed that the Kevlar panel partitions are sufficiently closely spaced to conform to the locally reacting impedance assumption.

The design of the SDOF panels is based on analytical models. The resistance is given by a model developed by Rice (Reference 5) for the effects of mean flow on a perforated plate:

$$R/\rho c = 0.3\ M/\sigma \tag{4.3-1}$$

where σ is the open area ratio (porosity) of the perforated plate. The reactance is given by the formula

$$\frac{X}{\rho c} = \frac{(t+\delta)\,\omega}{\sigma c} - \cot\left(\frac{\omega \ell}{c}\right) \tag{4.3-2}$$

where

$\omega = 2\pi f$

c = speed of sound

ℓ = cavity depth

t = faceplate thickness

and the orifice end correction is

$$\delta = \frac{.85d(1-.7\sqrt{\sigma})}{1+1.778\left(\frac{Mc}{200}\right)^3} \tag{4.3-3}$$

where d is the hole diameter.

These expressions resulted in a SDOF design with a cavity depth of 0.30 inches, covered by a 0.064-cm (0.025-inch) thick faceplate of 5.4% porosity (based also on availability). The hole diameter is 0.32 cm (0.125 in.) This gives a nominal impedance of 1.11-1.46i at the design Mach number of 0.2, compared to a design goal of 1.10-1.45i.

Table I summarizes the design parameters of the four different treatment panels. Figure 17 is a photograph of three completed treatment spool pieces, including a 5.1-cm (2-inch) Kevlar, the 10.2-cm (4-inch) SDOF, and a hard-wall filler.

Table I. Summary of Design Parameters of Treatment Test Panels

• LANGLEY DESIGN OPTIMIZATION

* Design frequency = 2740 Hz * $\eta = D/\lambda$ * m = 3 * m = 0.2

Configuration	Designation	Panel Impedances	Panel Construction	Predicted Suppression
2	10.2 cm (4") Single Phase Kevlar	1.10-1.45i (Design) 1.0-1.4i (Measured)	0.96 cm (0.38") Deep, 40% FP 2 Layers 'Fluffy' Over 2 Layers 'Dense'	44.3 dB
3	10.2 cm (4") Single Phase SDOF	1.1-1.45i (Design) 1.11-1.46i (Calculated)	0.76 cm (0.3") Deep 5.4% Faceplate	44.3 dB
4	5.1 cm + 5.1 cm (2"+2") Multiphase Kevlar 17.8 cm (7") Separation	0.525-1.40i (Design) 0.5-1.4i (Measured) (Downstream) 1.6-1.6i (Design) 1.6-1.6i (Measured) (Upstream)	1.02 cm (0.4") Deep 40% FP (Downstream) 0.84 cm (0.33") Deep 40% FP 4 Layers Dense (Upstream)	34.5 dB
5	5.1 cm (2") Single Phase Kevlar	0.525-1.40i (Design) 0.5-1.4i (Measured)	1.02 cm (0.4") Deep, 40% FP 2 Layers Fluffy	40.3 dB

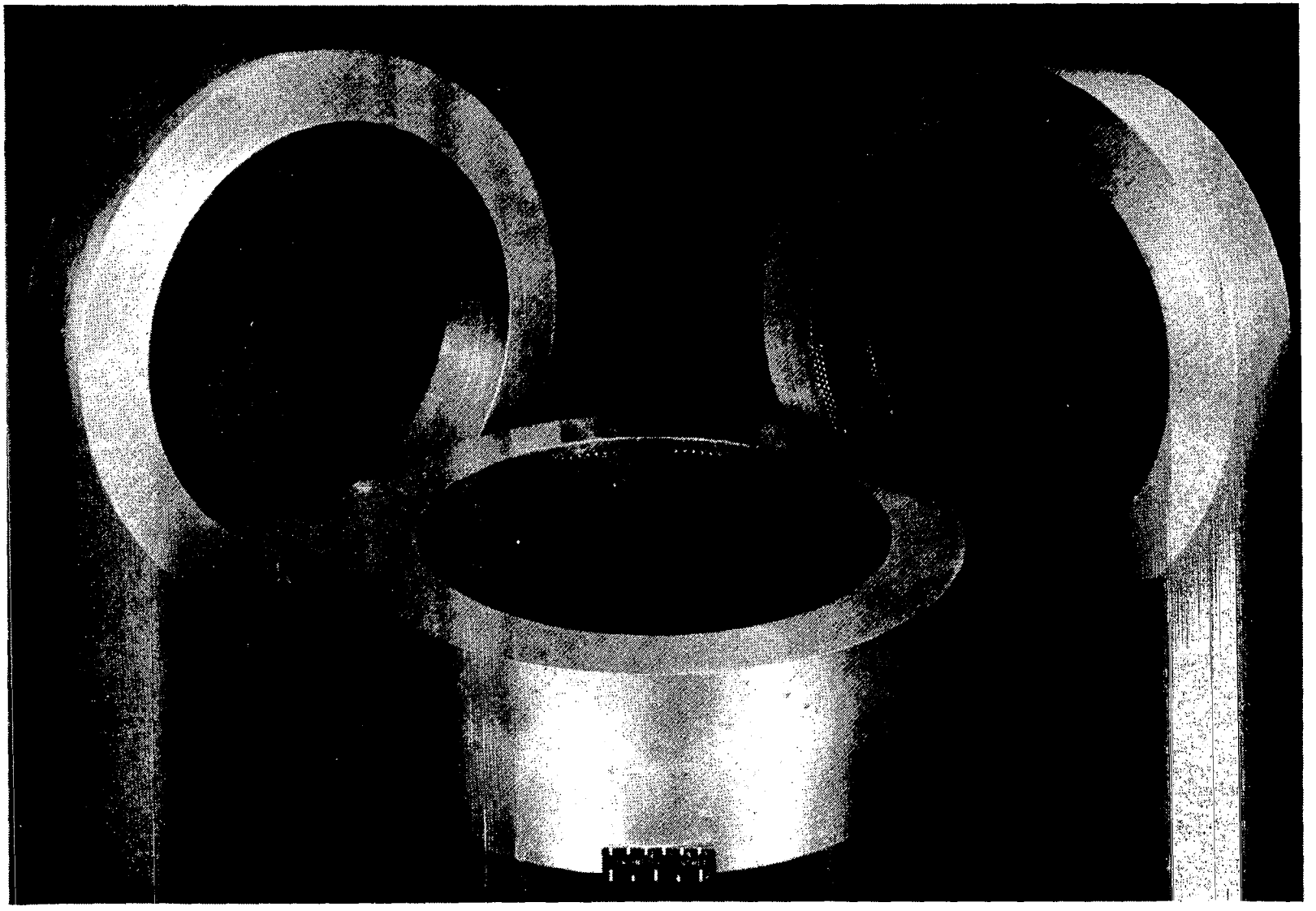

Figure 17. Treatment Spool Pieces.

5.0 INLET DUCT TESTS

A series of tests was conducted in the NASA-LRC ANRL Anechoic Chamber to measure the acoustic suppression of the treatment panel designs. The Spinning Mode Synthesizer Apparatus was used as a sound source for the tests. In addition to the design conditions, tests were run for variations in duct Mach number, spinning mode order, and excitation frequency. A total of five inlet configurations was tested, including the four treatment designs and a hard-wall baseline. The configuration designations are listed in Figure 18.

5.1 TEST PROGRAM AND APPARATUS

The inlet duct test apparatus was mounted in the side wall of the NASA-LRC ANRL Anechoic Chamber. The Anechoic Chamber measures 9.14-meters wide by 6.10-meters deep by 7.16-meters high. Figure 19 is a photograph of the duct test apparatus mounted in the chamber.

The test hardware, including treatment panels and in-duct instrumentation, was mounted in replaceable spool pieces which bolt to the duct flange mounted on the anechoic chamber wall. The inlet, designed by Professor P. Steven Barna of Old Dominion University, is specially contoured to provide a highly uniform flow profile at the entrance to the straight portion of the duct. The treatment panels are permanently mounted in 40.6-cm (16-inch) O.D. rings which are held in place by a 30.5-cm (12-inch) long split casing, as shown in Figure 20.

The in-duct acoustic instrumentation consisted of a circumferentially traversing, spinning-mode probe and four radially traversing probes. A schematic of the probe location is shown in Figure 21. The spinning-mode probe, developed under an earlier NASA-LRC/GE contract, (Reference 6), was modified by replacing the four immersed probes with flush-mounted transducers. The probe has four transducers mounted with 90° separation, can traverse a total of 180°, and can be set at arbitrarily small angular increments. The radial probes consist of 0.64-cm (0.25-inch) diameter straight stainless steel tubing with transducers flush-mounted at the tip. The acoustic probes can be replaced at any position with a Kiel-type total pressure probe for aerodynamic flow profile measurements.

Far-field acoustic SPL measurements were taken with a condenser microphone mounted on a traversing boom. The microphone was traversed in a horizontal arc at a 305-cm (10-ft) radius, from the center point at the face of the inlet, as shown in the photograph in Figure 22.

The sound source for the tests was the Spinning Mode Synthesizer, developed for NASA-Langley by Lockheed-Georgia. The synthesizer can be programmed to create a given spinning-mode pattern at an arbitrary pure-tone frequency. The device consists of 24 drivers arranged circumferentially about the duct with 48 flush-mounted transducers spaced circumferentially around the duct a short distance upstream of the drivers. The apparatus is pictured in Figure 23. A computer-controlled oscillator system sends input signals of

Configuration		Description
1	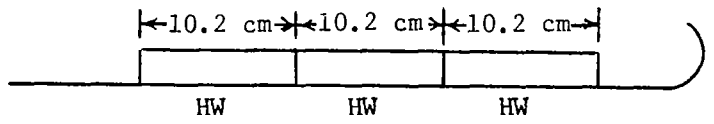	Hard Wall
2	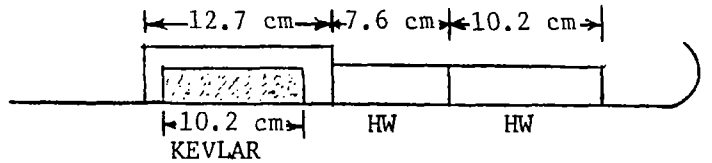	10.2 cm (4 in.) Single-Phase Kevlar
3	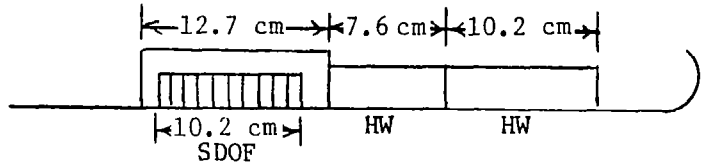	10.2 cm (4 in.) Single-Phase SDOF (Honeycomb + Perforated Plate)
4	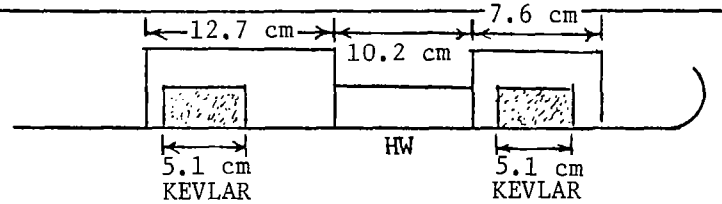	5.1 cm + 5.1 cm (2 in. + 2 in.) Multiphase Kevlar
5	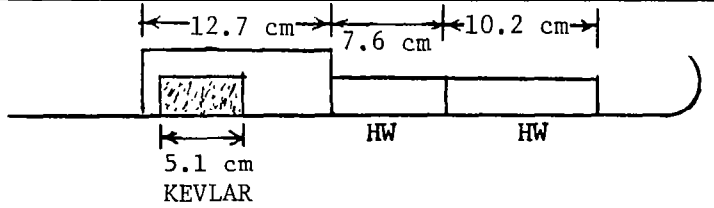	5.1 cm (2 in.) Single-Phase Kevlar

Figure 18. Treatment Design and Test Configurations.

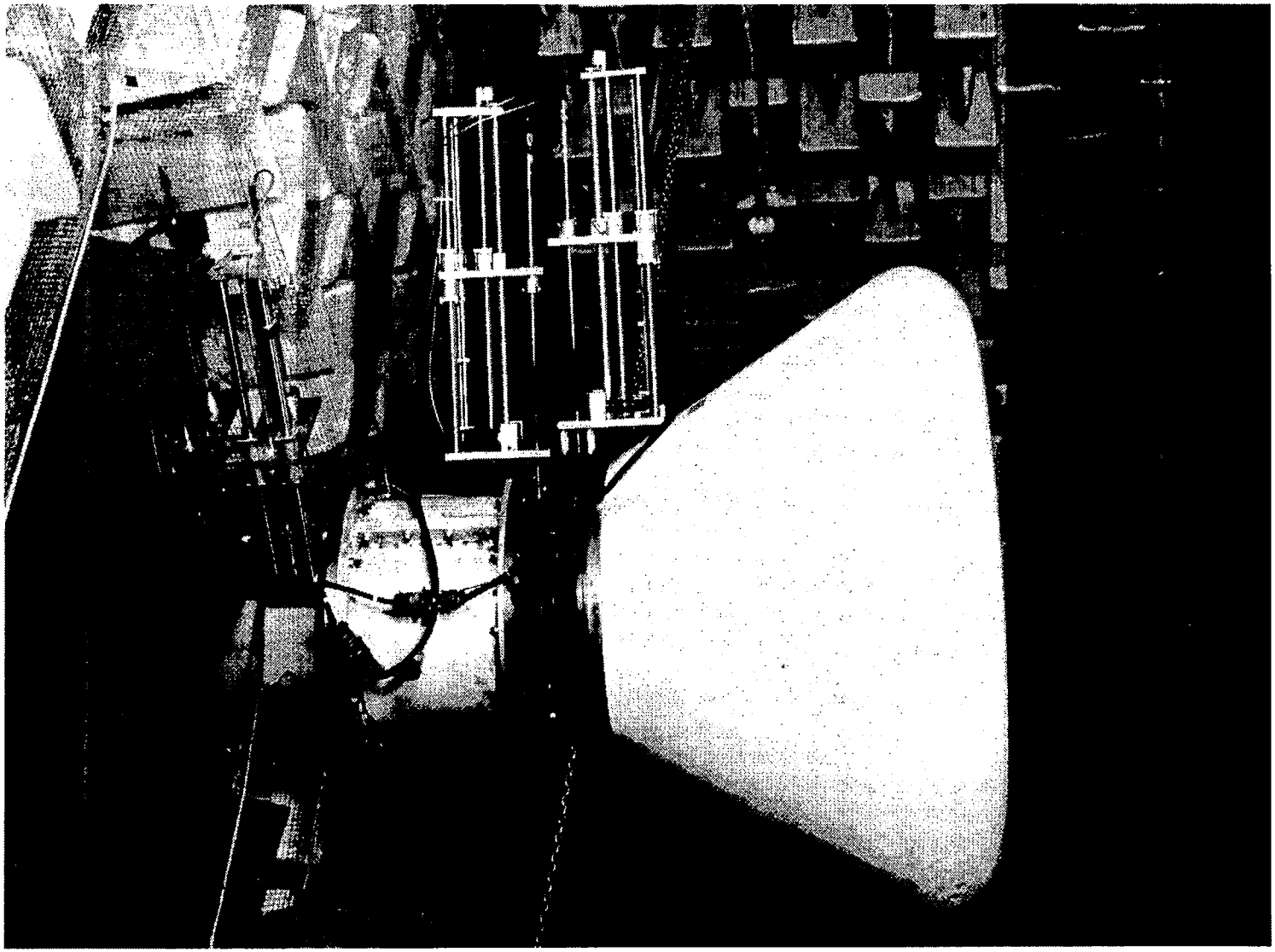

Figure 19. Duct Test Apparatus Mounted in Chamber.

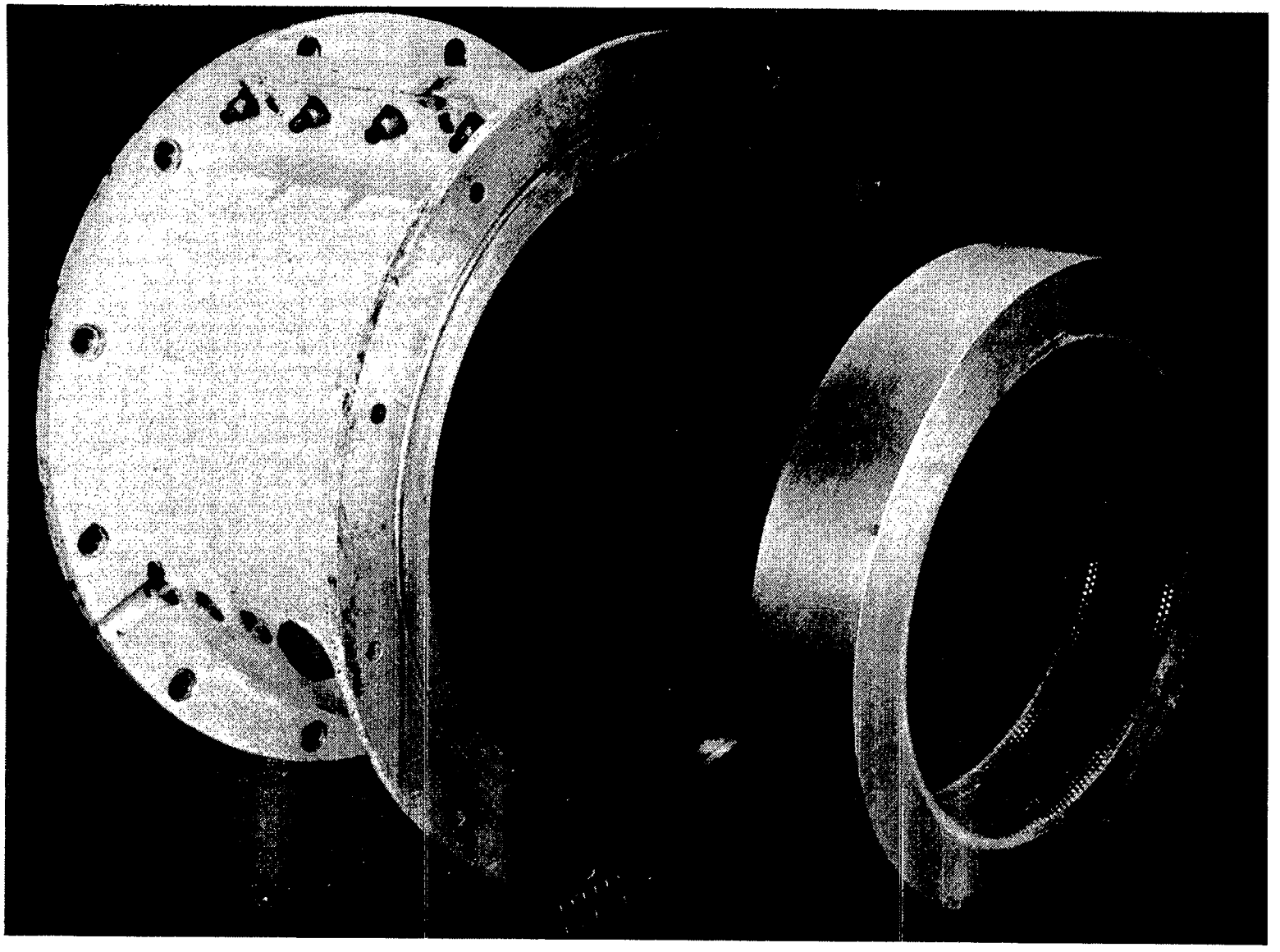

Figure 20. Treatment Panels Mounted in Rings.

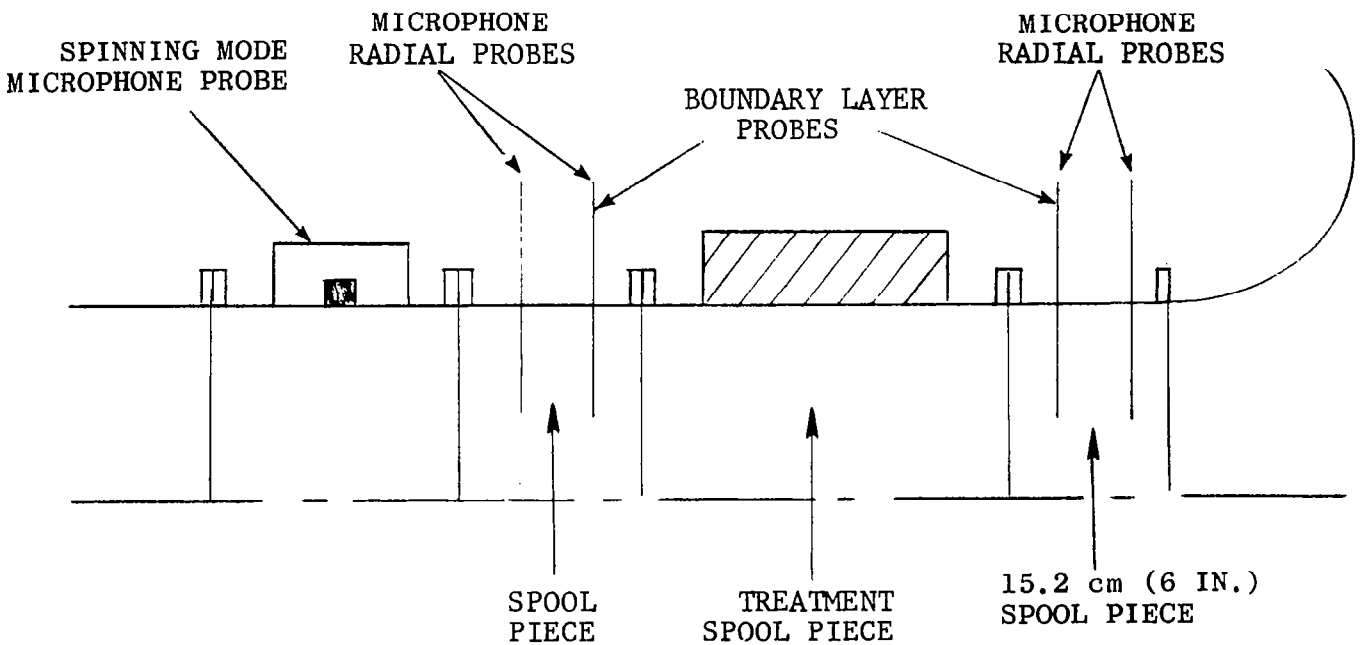

Figure 21. Schematic of Inlet Duct Test In-Duct Instrumentation Locations.

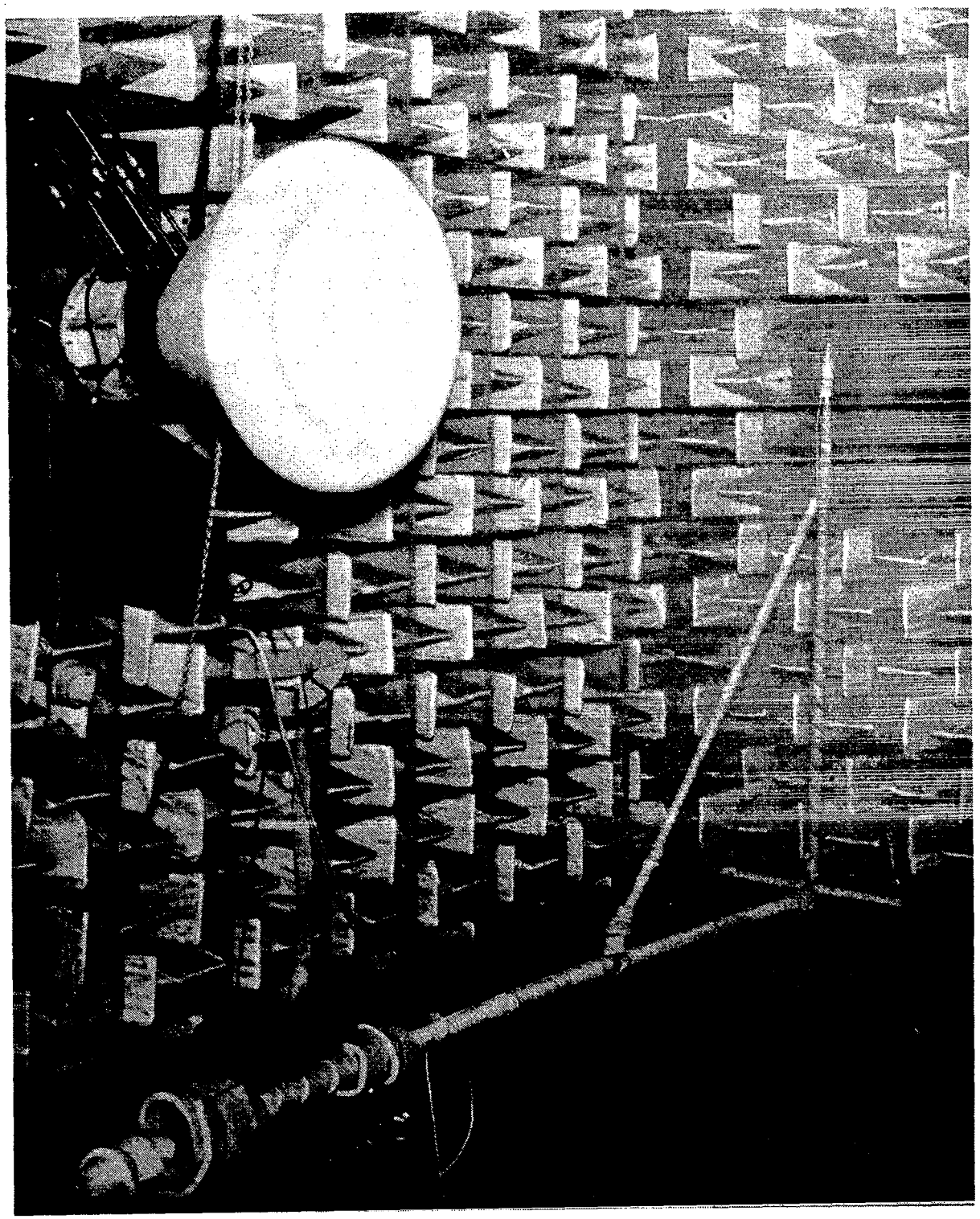

Figure 22. Far-Field Traverse Microphone Boom.

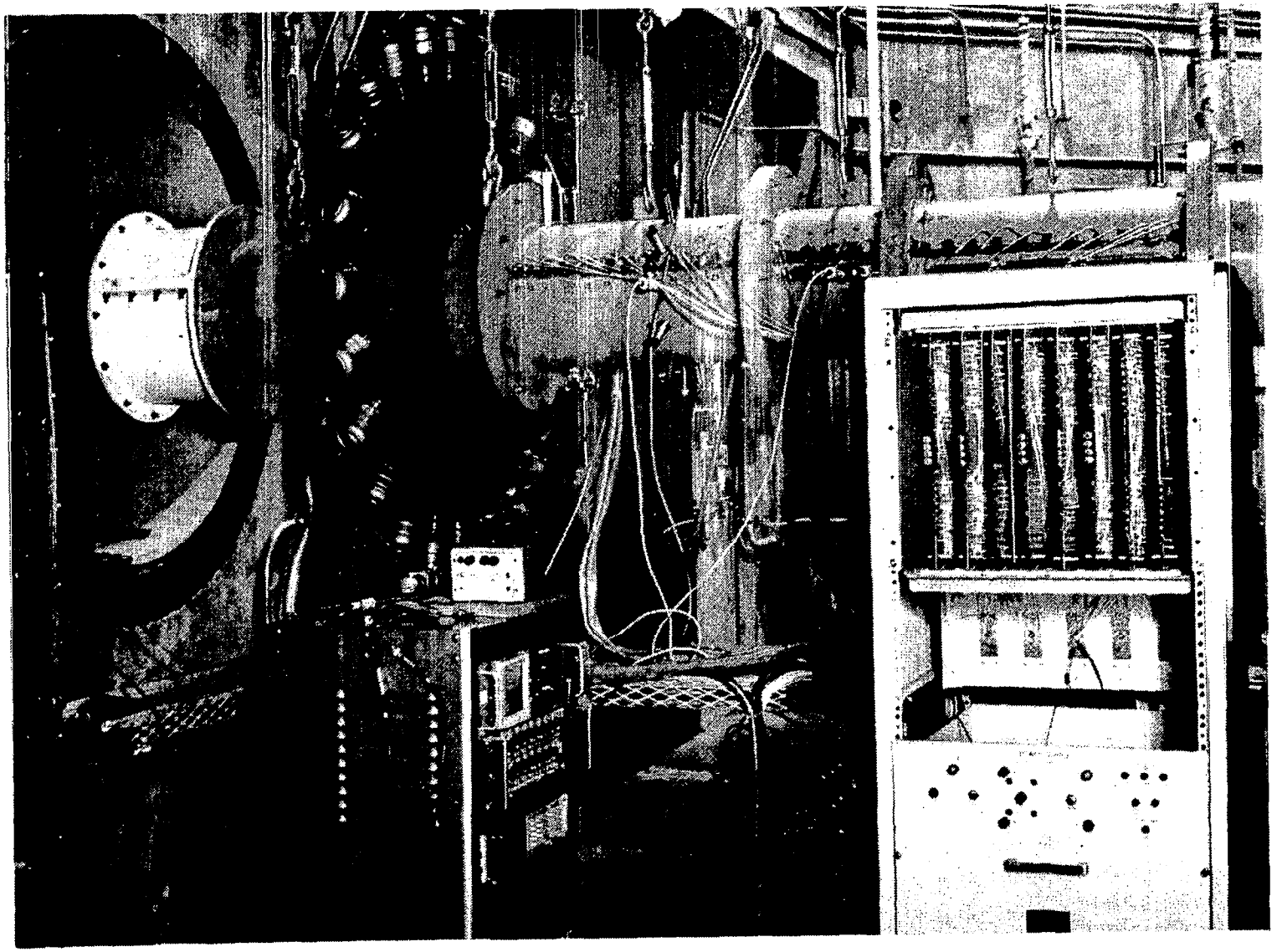

Figure 23. NASA-Langley Spinning Mode Synthesizer.

prescribed amplitude and phase to each of 24 individual amplifiers for the drivers. The 48 microphones measure the output of the drivers in the duct and provide input signals to the computer for analysis of the spinning mode content. A computerized iteration program then calculates corrections to the input signals which will adjust the output of each of the drivers toward the desired spinning mode. The feedback iteration procedure is repeated until the output spinning mode pattern is achieved within a desired level of error.

Eleven different runs were made for each of the five treatment configurations. Each run consisted of a different combination of spinning mode order, excitation frequency, and Mach number, as listed in Table II. For each run, in-duct spinning-mode measurements, in-duct radial-mode measurements, and far-field measurements were made. All data were acquired on-line, using a computer-based analog/digital (A/D) data acquisition/reduction system to be described in the next section.

5.2 DATA ACQUSITION/REDUCTION PROGRAMS

Acoustic data acquisition and reduction for the spinning mode probe, the radial probes, and the far-field microphone were accomplished on-line using a two-channel analog-to-digital converter controlled by a minicomputer. The signals from the spinning mode and radial probes were conditioned using low-noise differential amplifiers. The data acquisition and reduction programs were developed specifically for these tests and were programmed in Fortran language.

The operation of the spinning mode probe has been described in a previous report (Reference 6). Basically, it is the measurement of the spatial pattern of the acoustic pressure cross-spectrum around a circumferential line at a constant duct radius. The cross-spectrum is calculated at the excitation frequency using the electronic signal from the Spinning Mode Synthesizer master oscillator as a reference. The spatial complex acoustic pressure pattern is analyzed into component spinning modes using a Fourier-type expansion:

$$p(\theta) = \sum_{m=-N}^{N} A_m e^{im\theta} \qquad (5.2\text{-}1)$$

where θ is the angular variable, A_m is the m-th complex modal coefficient, $p(\theta)$ is the measured acoustic pressure cross-spectrum, and N is the maximum spinning-mode order under consideration. The entire data acquisition/reduction program was automated on the minicomputer; therefore, the spinning mode decomposition was available almost immediately upon completion of the measurement.

The radial measurements are made at four planes: two planes upstream of the treatment section and two planes downstream. Each pair of traversing probes is used in a modal measurement technique which separates forward- and backward-traveling waves in the presence of higher order radial modes.

Table II. Inlet Test Run Designation for Each Configuration

Run Number	Spinning Mode Order	Mach Number	Frequency, Hz
1	3	0	2740
2	3	.3	2740
3	3	.2	2740
4	2	.2	2740
5	0	.2	2740
6	3	.2	1570
7	0	.2	1570
8	3	.2	2150
9	0	.2	2150
10	3	.2	3250
11	0	.2	3250

Since the radial traverses are made at only one circumferential position, it must be assumed that only one spinning mode order, with modes spinning in only one direction, is present. It was hoped that this condition could be achieved with the Spinning Mode Synthesizer.

The forward/backward-wave separation requires radial traverses at two closely spaced axial positions in a hard-wall section of duct, as illustrated in Figure 24. The measured cross-spectrum as a function of radial position at Plane 1 can be expanded in terms of Bessel Function as

$$p_1(r) = \sum_{j=1}^{N} \left[A_j J_m \left(\gamma^+_{mj} \frac{r}{B} \right) + B_j e^{-i\kappa^-_{mj}\ell} J_m \left(\gamma^-_{mj} \frac{r}{B} \right) \right] \qquad (5.2\text{-}2)$$

where

p = Measured cross-spectrum of acoustic pressure

r = Radial variable

j = Radial mode index

N = Number of radial modes in expansion

A_j = Forward modal coefficient

m = Spinning mode order

$\gamma^{\pm}_{mj}$ = Mode eigenvalues for hard-wall duct

B = Duct radius

B_j = Backward mode coefficient

Similarly, at Plane 2,

$$p_2(r) = \sum_{j=1}^{N} \left[A_j e^{im\Delta\Theta} e^{i\kappa^+_{mj}\ell} J_m \left(\gamma^+_{mj} \frac{r}{B} \right) + B_j e^{im\Delta\Theta} J_m \left(\gamma^-_{mj} \frac{r}{B} \right) \right] \qquad (5.2\text{-}3)$$

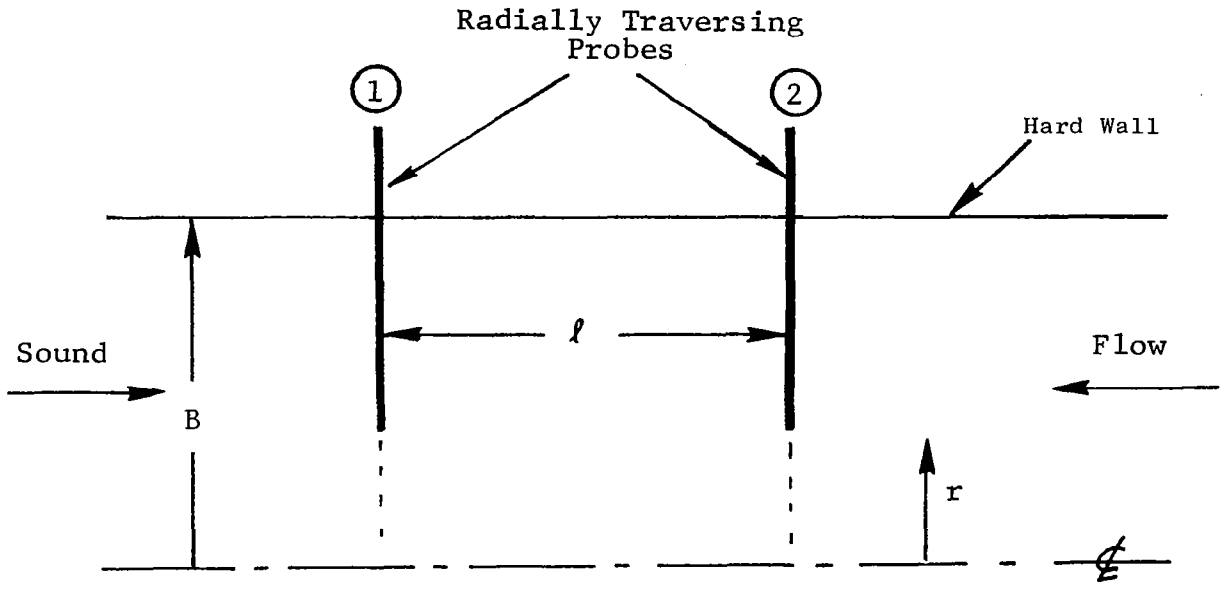

Figure 24. Two-Plane, Forward/Backward-Wave Separation Measurement System.

where $\Delta\theta$ is the circumferential angular separation between the two radial traverses. The axial propagation constants in the hard-wall section of duct are given by

$$\frac{\kappa^{\pm}_{mj}}{k} = \frac{-M \pm \sqrt{1 - (1-M^2)\left(\frac{\gamma^{\pm}_{mj}}{kB}\right)^2}}{1 - M^2} \tag{5.2-4}$$

The eigenvalues must take into account any effects of boundary layers, if present.

The objective is to solve for the 2N unknowns A_j and B_j. A set of equations in matrix form is obtained by multiplying Equation 5.2-2 through by r times the forward-mode eigenfunction and integrating from 0 to B,

$$\int_0^B p_1(r)\, J_m\left(\gamma^+_{mn}\frac{r}{B}\right) r\, dr =$$

$$\sum_{j=1}^{N}\left[A_j \int_0^B J_m\left(\gamma^+_{mj}\frac{r}{B}\right) J_m\left(\gamma^+_{mn}\frac{r}{B}\right) r\, dr + B_j e^{-i\kappa^-_{mj}\ell} \int_0^B J_m\left(\gamma^-_{mj}\frac{r}{B}\right) J_m\left(\gamma^+_{mn}\frac{r}{B}\right) r\, dr\right] \tag{5.2-5}$$

and multiplying Equation 5.2-3 through by r times the backward-mode eigenfunction and integrating,

$$\int_0^B p_2(r)\, J_m\left(\gamma^-_{mn}\frac{r}{B}\right) r\, dr =$$

$$\sum_{j=1}^{N}\left[A_j e^{im\Delta\Theta} e^{i\kappa^+_{mj}\ell} \int_0^B J_m\left(\gamma^+_{mj}\frac{r}{B}\right) J_m\left(\gamma^-_{mn}\frac{r}{B}\right) r\, dr + B_j e^{im\Delta\Theta} \int_0^B J_m\left(\gamma^-_{mj}\frac{r}{B}\right) J_m\left(\gamma^-_{mn}\frac{r}{B}\right) r\, dr\right] \tag{5.2-6}$$

These equations can be expressed in matrix form as

$$\begin{Bmatrix} P_{1,1^+} \\ P_{2,1^-} \\ P_{1,2^+} \\ P_{1,2^-} \\ \vdots \\ P_{1,N^+} \\ P_{2,N^-} \end{Bmatrix} = \begin{bmatrix} G_{1^+1^+} & G_{1^+1^-} & G_{1^+2^+} & G_{1^+2^-} & \cdots\cdots\cdots & G_{1^+N^+} & G_{1^+N^-} \\ G_{1^-1^+} & G_{1^-1^-} & G_{1^-2^+} & G_{1^-2^-} & \cdots\cdots\cdots & & \\ G_{2^+1^+} & G_{2^+1^-} & G_{2^+2^+} & \cdots\cdots\cdots & & & \\ G_{2^-1^+} & \cdots\cdots\cdots & & & & & \\ \vdots & & & & & & \\ G_{N^+1^+} & G_{N^+1^-} & \cdots\cdots\cdots\cdots\cdots\cdots & & & G_{N^+N^+} & G_{N^+N^-} \\ G_{N^-1^+} & G_{N^-1^-} & & & & G_{N^-N^+} & G_{N^-N^-} \end{bmatrix} \begin{Bmatrix} A_1 \\ B_1 \\ A_2 \\ B_2 \\ \vdots \\ A_N \\ B_N \end{Bmatrix} \tag{5.2.7}$$

where

$$P_{1,1^+} = \int_0^B p_1(r)\ J_m\left(\gamma^+_{m1}\frac{r}{B}\right)\ r\ dr \tag{5.2-8}$$

etc., and

$$G_{1^+1^+} = \int_0^B J_m\left(\gamma_{m1}^+ \frac{r}{B}\right) J_m\left(\gamma_{m1}^+ \frac{r}{B}\right) r\, dr \qquad (5.2\text{-}9)$$

etc. The P integrals are determined by numerical integration, the G integrals are known from closed form integrals of products of Bessel functions, and the coefficients in the matrix equation are found by ordinary matrix-solution methods.

The far-field traverse again utilizes the computerized data acquisition system. The far-field sound power levels are calculated by two different methods. First, at each microphone angular position the acoustic pressure narrowband autospectrum is converted to SPL and integrated around a hemisphere assuming cylindrical symmetry. Second, the narrowband cross-spectrum between each far-field microphone and the Spinning Mode Synthesizer master oscillator reference signal is converted to SPL and integrated about the hemisphere. By forming the far-field PWL's from the cross-spectrum, the levels of far-field radiated, pure-tone sound which are coherent with the source can be extracted from incoherent noise present in the same narrowband, thus, improving the signal-to-noise ratio. In addition, it is possible to plot the relative phase of the far-field radiation pattern, a quantity seldom considered in evaluating far-field results.

Treatment suppression is obtained from the far-field data by integrating the measured SPL's about a hemisphere to form sound power levels. Since only a 90° traverse is required for this calculation, whereas the microphone boom traverses a total of 180°, two calculated values of PWL are found. One uses data from -90° to 0°; the other uses data from 0° to 90° These calculations are performed for the cross-spectral measurements.

5.3 RESULTS OF INLET TREATMENT TESTING

For each run of each Configuration, the following data are of importance:

- In-duct measured spinning mode content.
- In-duct measured ΔPWL from forward/backward-wave separation.
- Far-field continuous traverse SPL radiation patterns.
- Far-field autospectral and cross-spectral ΔPWL's, hard wall versus treated.

Plots of spinning mode relative levels are shown for each of the five configurations in Figures 25 through 29. Plots of far-field continuous traverses are shown in Figures 30 through 33. The far-field traverses for the treated configurations are compared to the hard-wall traverse in each case. All planned runs except 2 and 4 of Configurations 3, 4, and 5 were completed within the allotted test time.

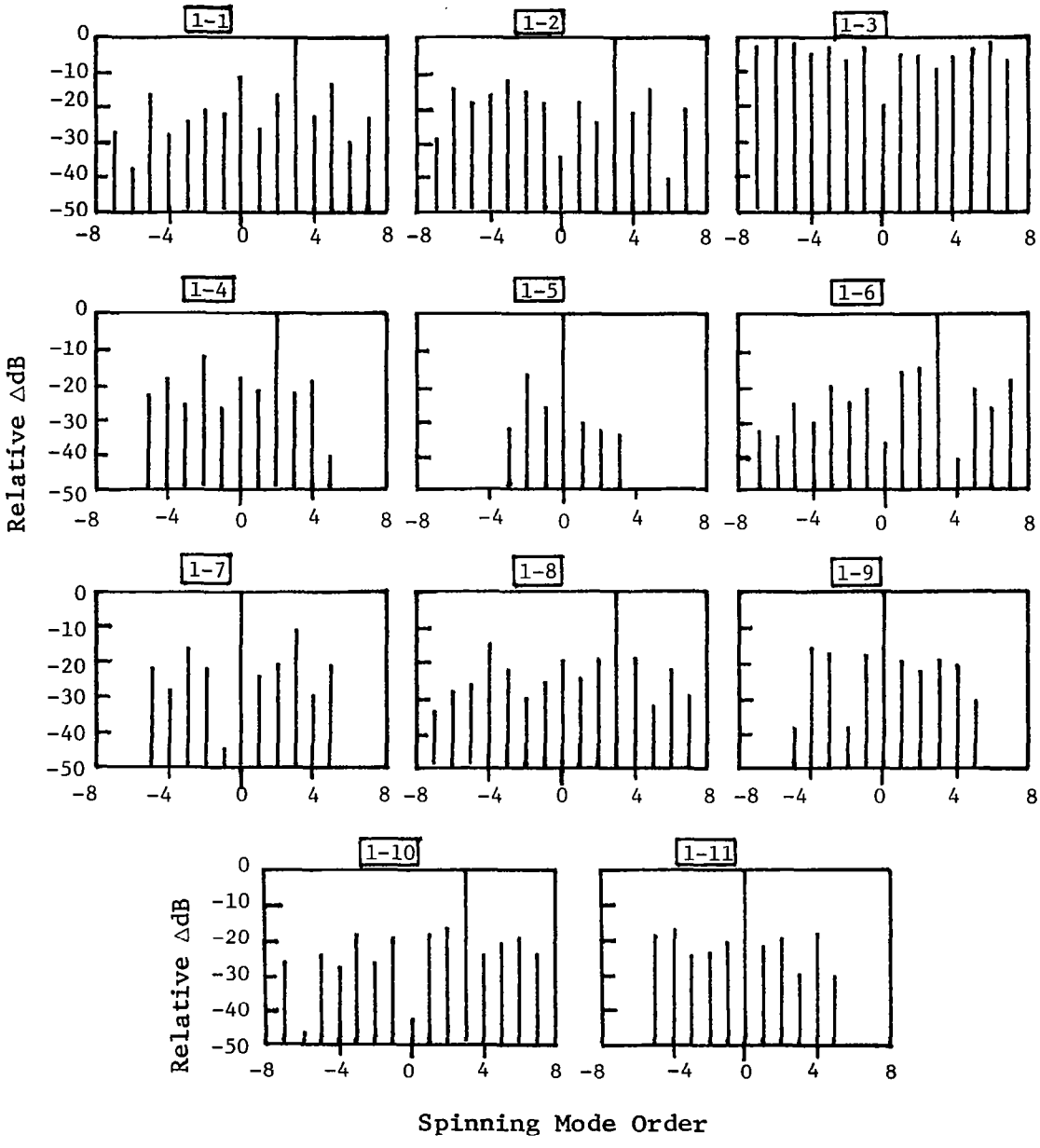

Figure 25. Relative Spinning Mode Levels Measured by Spinning Mode Probe, Configuration 1.

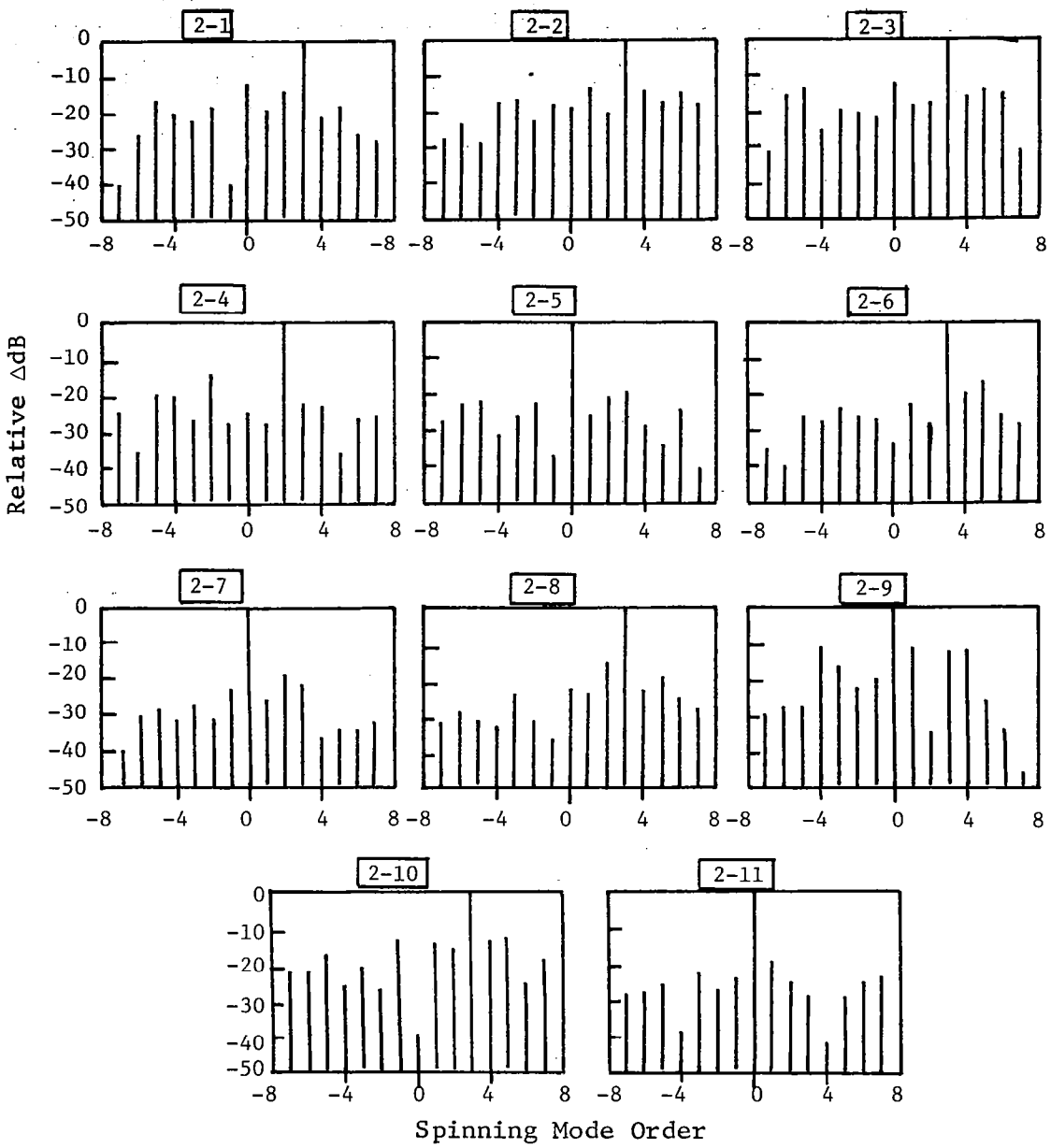

Figure 26. Relative Spinning Mode Levels Measured by Spinning Mode Probe, Configuration 2.

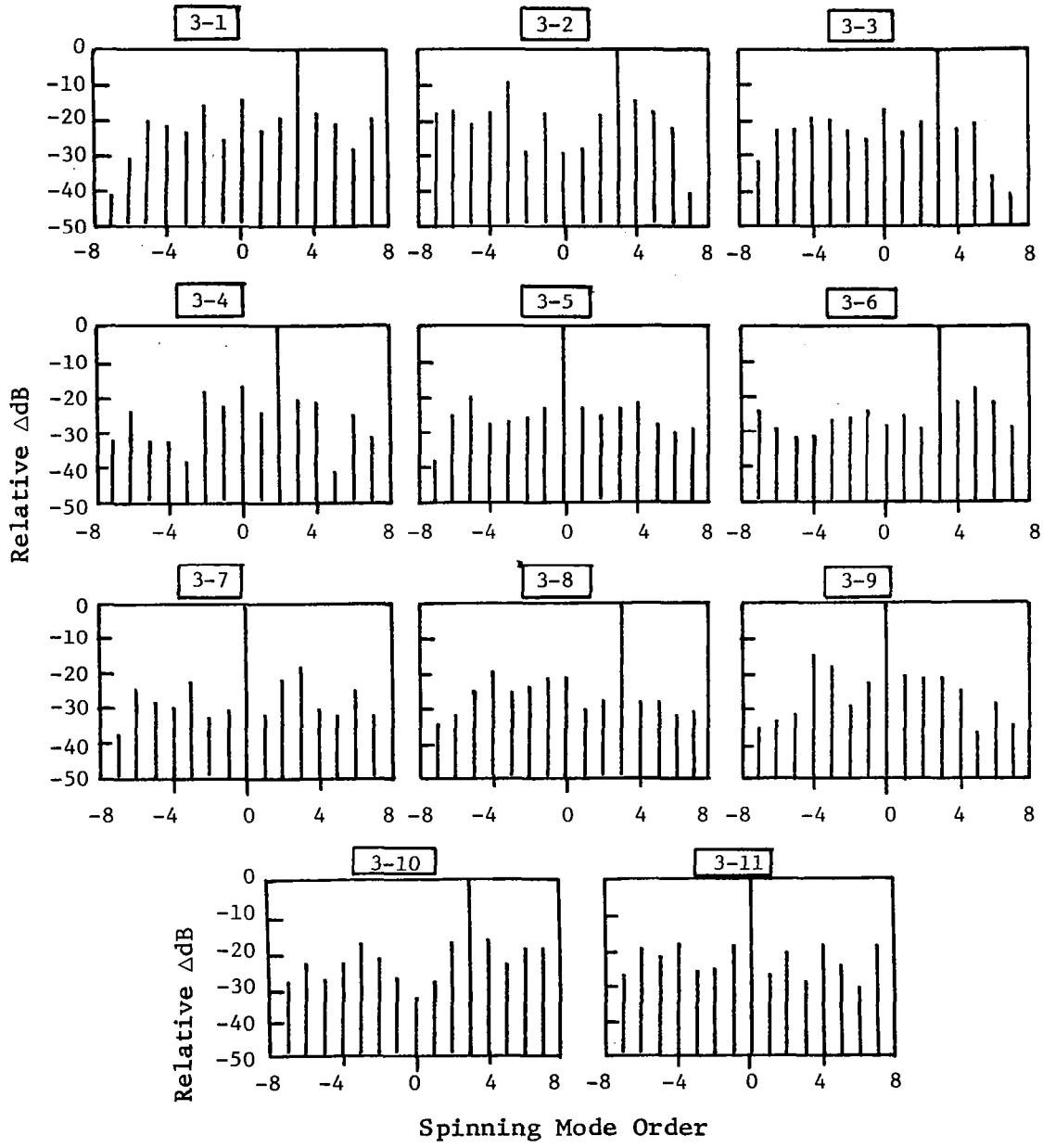

Figure 27. Relative Spinning Mode Levels Measured by Spinning Mode Probe, Configuration 3.

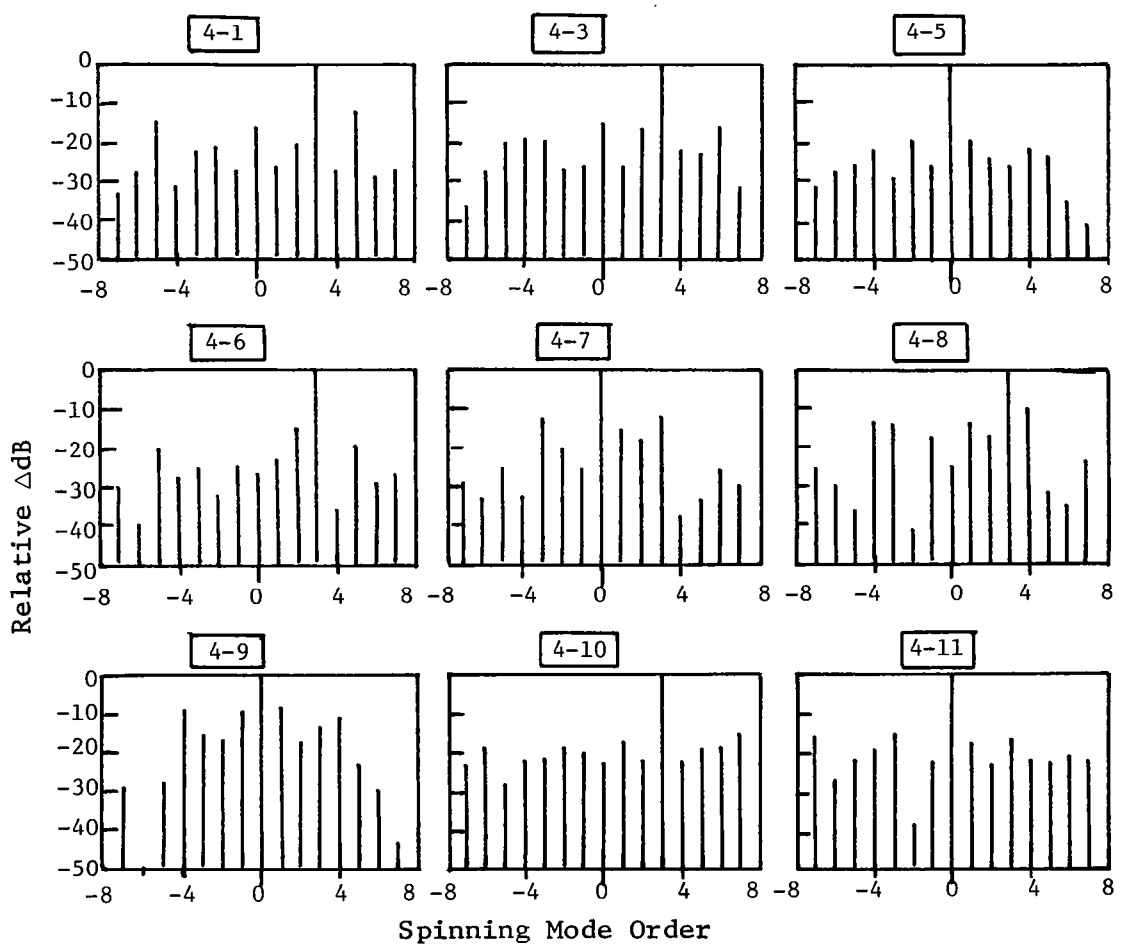

Figure 28. Relative Spinning Mode Levels Measured by Spinning Mode Probe, Configuration 4.

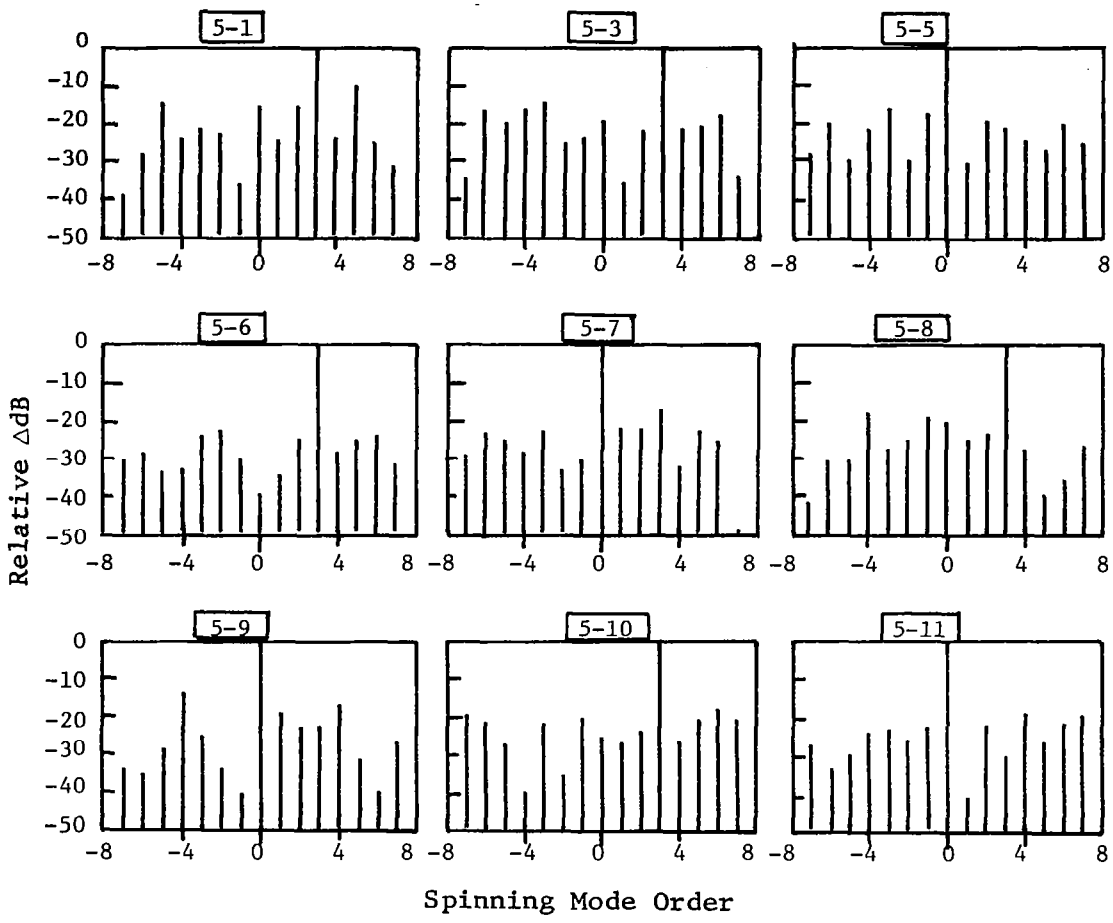

Figure 29. Relative Spinning Mode Levels Measured by Spinning Probe, Configuration 5.

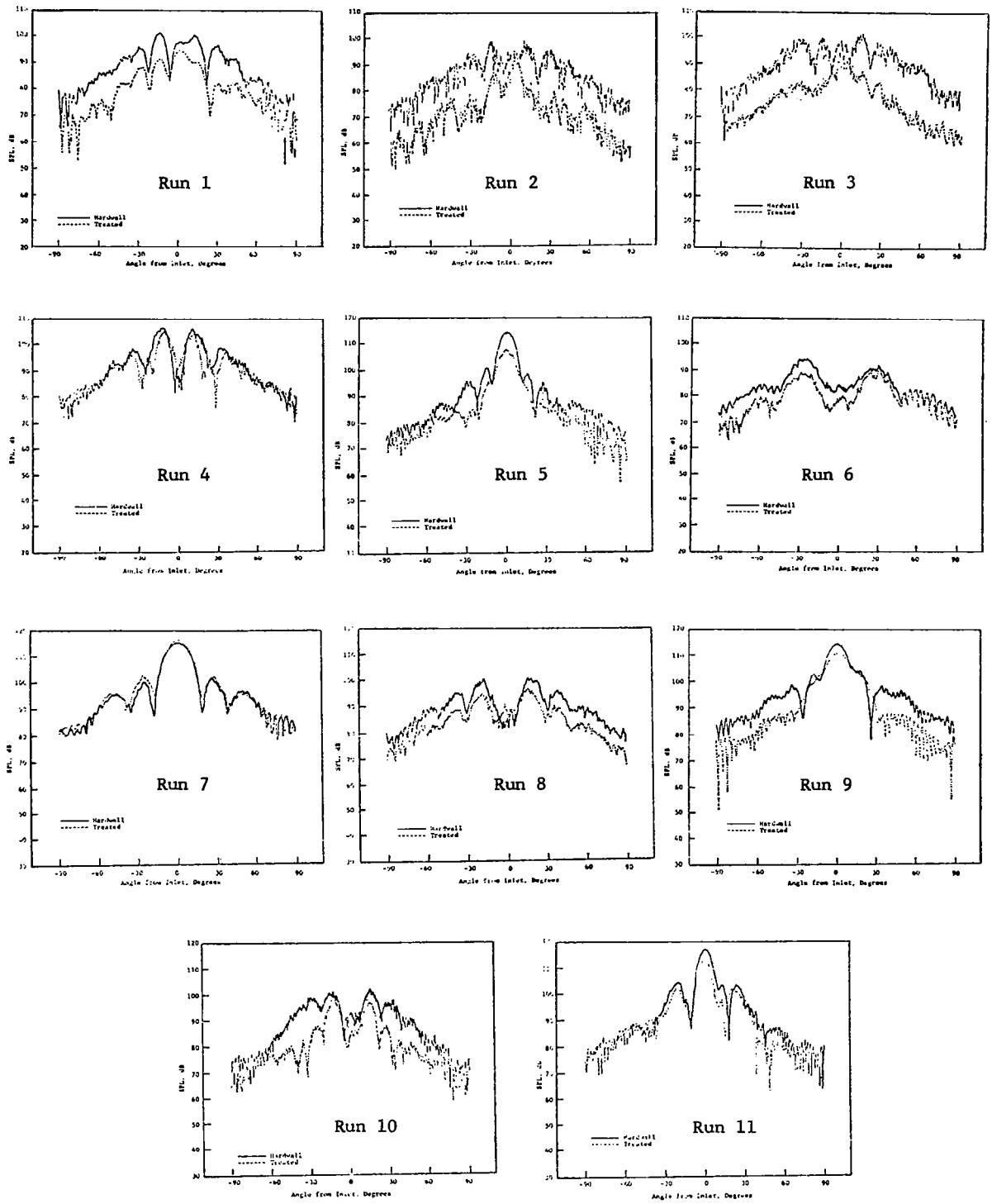

Figure 30. Comparison of Hard-Wall and Treated Far-Field Continuous Traverses, Configuration 2.

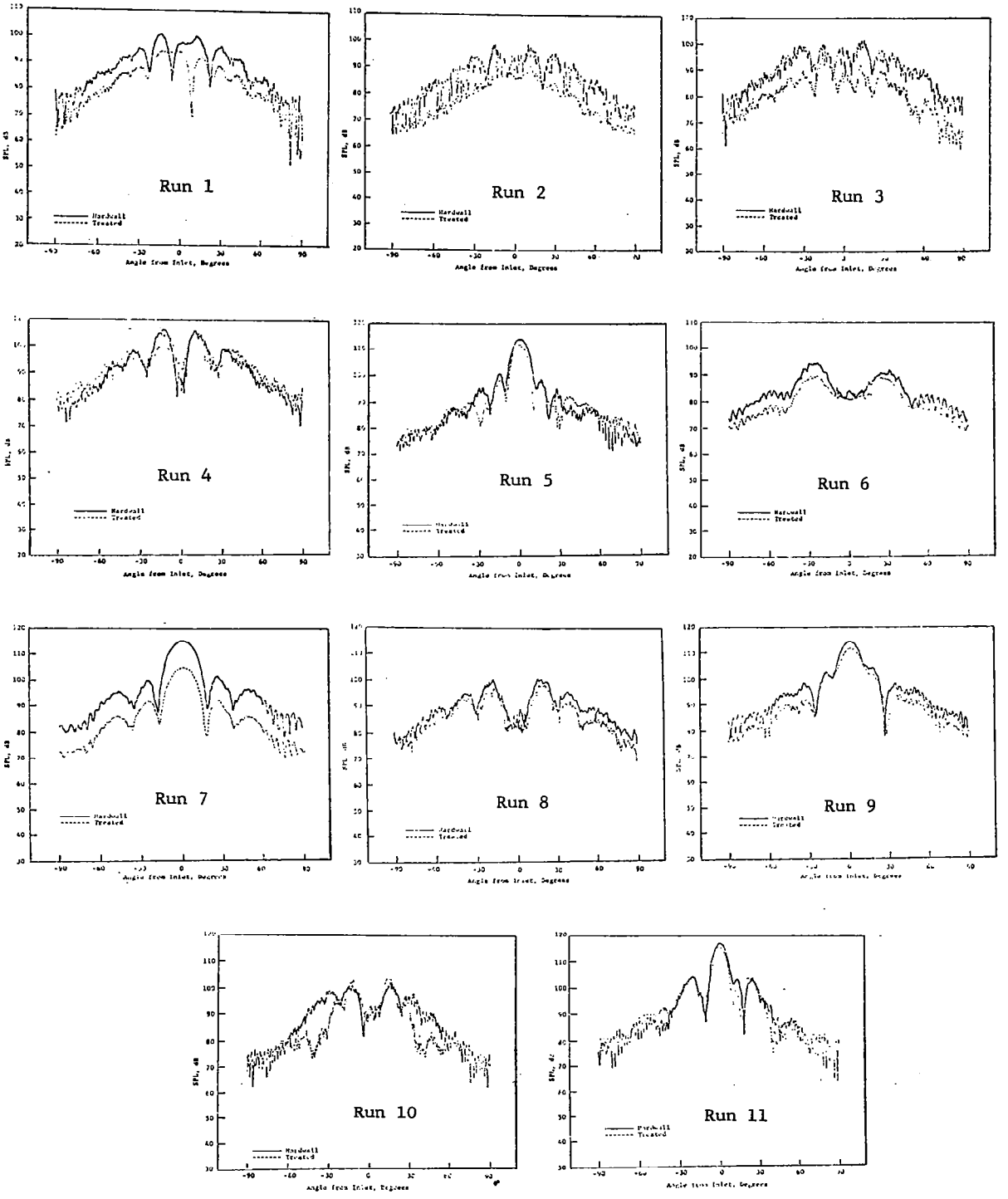

Figure 31. Comparison of Hard-Wall and Treated Far-Field Continuous Traverses, Configuration 3.

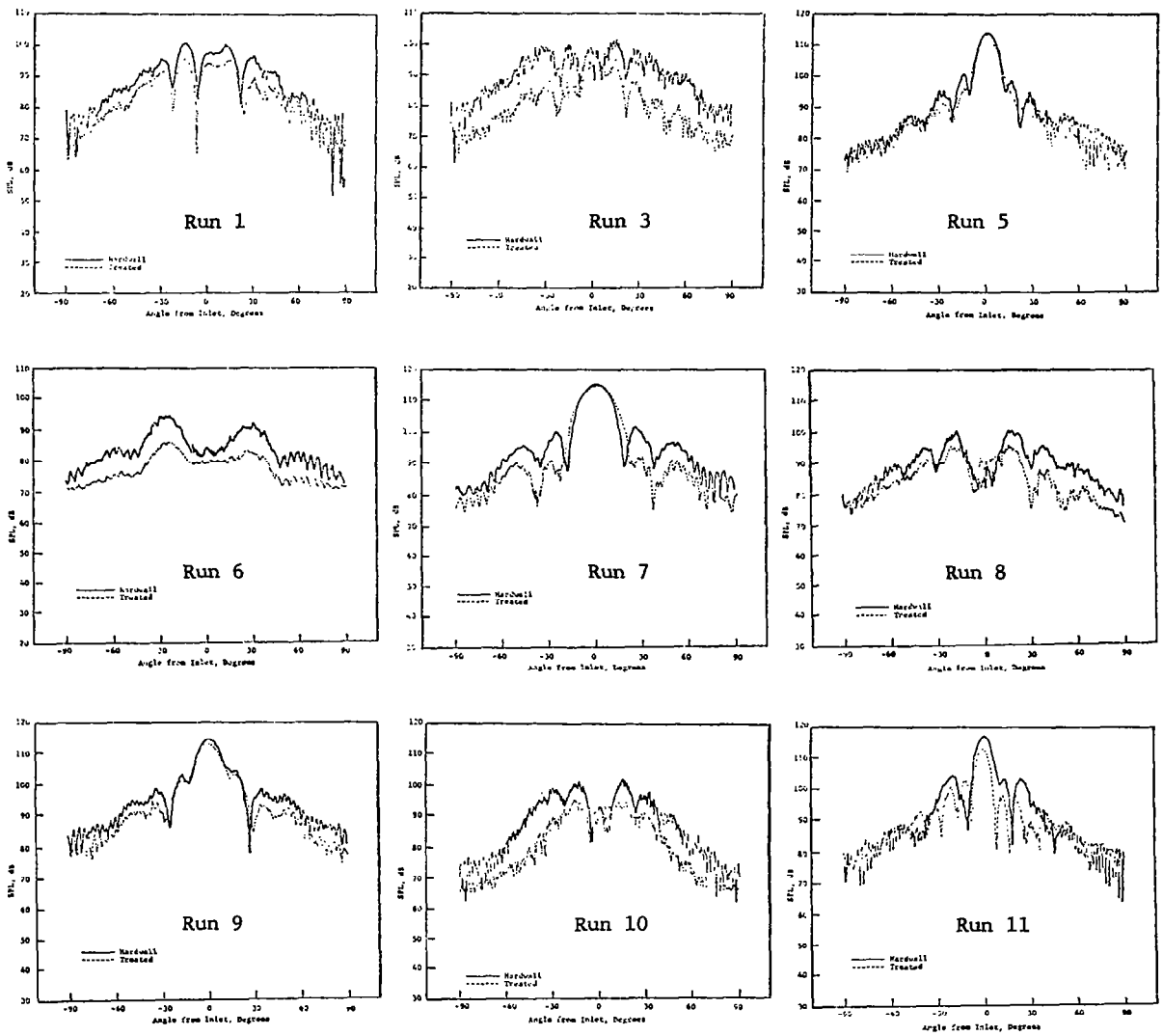

Figure 32. Comparison of Hard-Wall and Treated Far-Field Continuous Traverses, Configuration 4.

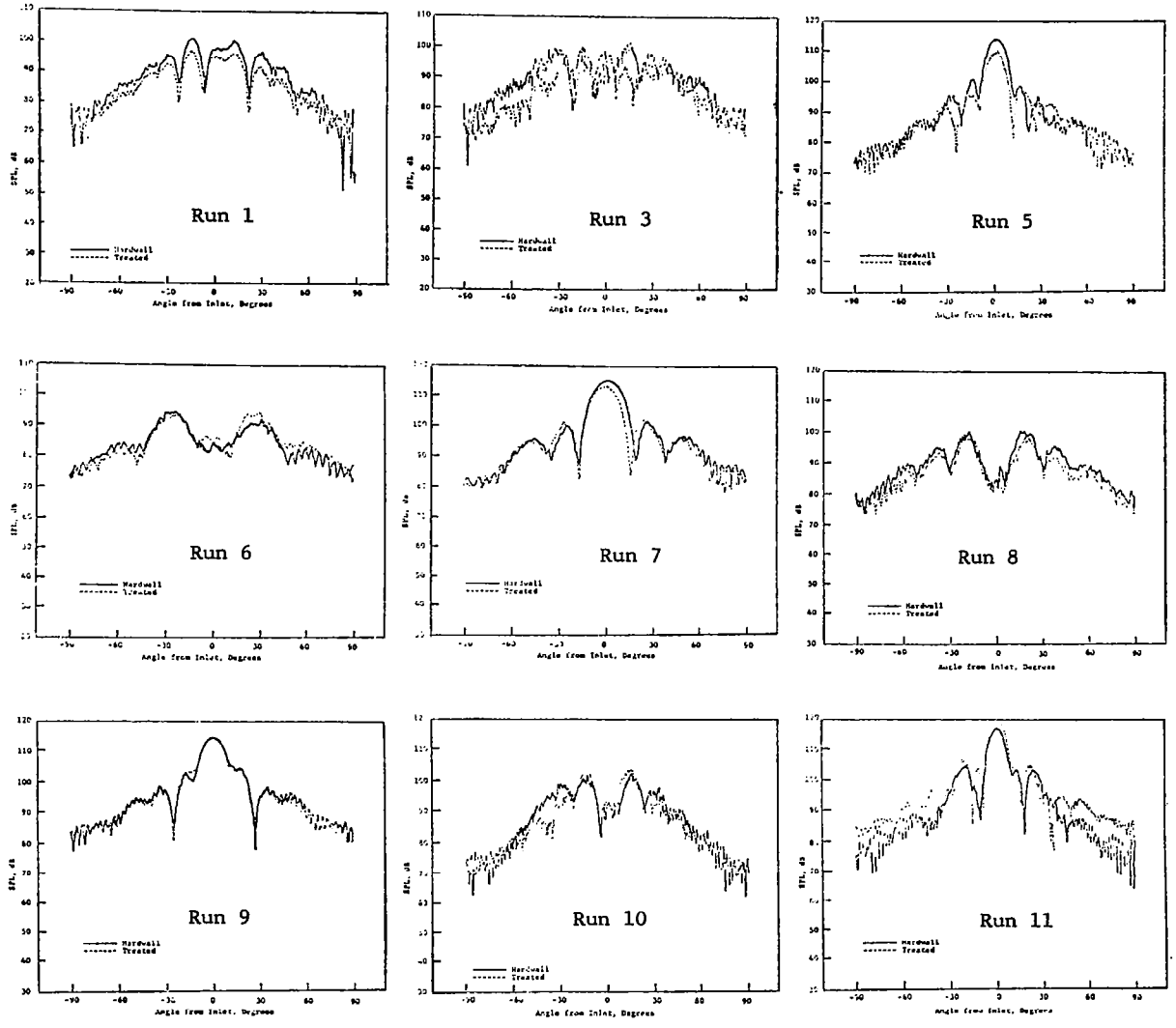

Figure 33. Comparison of Hard-Wall and Treated Far-Field Continuous Traverses, Configuration 5.

6.0 COMPARISON OF PREDICTED AND MEASURED SUPPRESSION

6.1 RESULTS OF ANALYTICAL PREDICTIONS

Predictions were made of the suppression for each of the configurations. The predictions were based on the measured, forward-traveling, radial-mode content at the source plane, assuming the desired spinning-mode order was the only one present. The impedances used for the treatment panels are those presented in Table III: standing-wave-tube measured values in the case of the Kevlar panels and analytical values in the case of the SDOF panel.

Tables IV through VII present a listing of the predicted and measured suppression for each of the 11 runs for Configurations 2 to 5. Due to the failure of the boundary layer effects calculation to converge on the correct eigenvalues (although the correct uniform flow eigenvalues were obtained), the predictions were not obtained in several cases. Figures 34 through 37 compare predicted and measured suppression as a function of frequency for each configuration, for the m = 0 and m = 3 spinning mode orders at Mach 0.2.

6.2 PREDICTED VERSUS MEASURED RESULTS

From Tables IV to VII and Figures 34 through 37 it can be seen that there are cases in which the predicted and measured suppression are in close agreement (within 2 - 3 dB), but there are many cases in which agreement is not close. It is also apparent that the two methods of suppression measurement disagree substantially in many cases. The explanation of the variation in predicted and measured suppression among the two measured and the predicted values requires examination of the possible sources of error in the measurement and prediction.

One of the basic assumptions for both the measurement and the prediction was that modes of only a single spinning-mode order were present, and these modes were to be spinning in only the positive direction. In practice, the desired modes were always dominant, but the quality of the results was dependent on just how far the dominant mode was above other, unwanted, spinning-mode orders. Errors in both the measured suppression and the predicted suppression can be caused by the presence of unwanted spinning mode orders, due to the assumption of a pure spinning mode in the radial probe forward/backward wave separation modal measurement. In addition, errors in expected values of liner impedance can cause large variations in suppression near the design point, and some deviation can be expected due to the approximate nature of the boundary layer effects calculations.

Errors caused by the presence of extraneous spinning-mode orders are most extreme in the optimum design cases, that is, Run 3 of Configurations 2, 3, 4, and 5, the predicted suppressions are about 20 dB higher than the measured. In all of these cases, the m = 0 spinning mode is sufficiently high with respect to the m = +3 levels to contribute to the results. One indication of

Table III. Impedances Used for Calculation of Predicted Suppression

Treatment Configuration	Impedance			
	1570 Hz	2150 Hz	2740 Hz	3250 Hz
2	0.98-2.47i	0.71-1.63i	1.04-1.44i	1.19-1.05i
3	1.1-4.91i	1.1-3.39i	1.1-1.45i	1.1-2.18i
4 Upstream	2.52-3.47i	2.03-2.21i	1.62-1.56i	1.88-1.39i
4 Downstream	1.06-3.32i	0.53-1.83i	0.48-1.35i	0.4-1.16i
5	1.06-3.32i	0.53-1.83i	0.48-1.35i	0.4-1.16i

Table IV. Summary of Predicted and Measured Suppression, Configuration 2

Run Number	Spinning Mode Order	Frequency, Hz	Mach Number	Far-field ΔPWL, dB			In-Duct Modal Meas ΔPWL, dB	Predicted ΔPWL, dB
				-90° 0°	0° 90°	Avg		
1	3	2740	0	Data Lost			12.1*	-10
2	3	2740	0.3	- 7.60	-10.1	- 8.8	BAD	-11.6
3	3	2740	0.2	-10.40	-10.1	-10.3	BAD	-30.8
4	2	2740	0.2	- 3.80	- 2.1	- 2.95	- 1.0*	- 2.3
5	0	2740	0.2	- 6.40	- 6.1	- 6.30	BAD	- 3.9
6	3	1570	0.2	- 3.40	- 7.5	- 5.45	- 6.5	- 8.2
7	0	1570	0.2	+0.25	+ 0.07	+ 0.16	- 1.0	---
8	3	2150	0.2	-5.50	- 6.6	- 6.10	- 7.9	-12.4
9	0	2150	0.2	-3.80	-4.75	- 4.30	- 2.1*	-11.5
10	3	3250	0.2	-9.50	-13.40	-11.5	- 8.6	- 8.5
11	0	3250	0.2	-3.10	- 2.5	- 2.8	BAD	- 1.6

*Measurement Accuracy Questionable

Table V. Summary of Predicted and Measured Suppression, Configuration 3

Run Number	Spinning Mode Order	Frequency, Hz	Mach Number	Far-field ΔPWL, dB			In-Duct Modal Meas ΔPWL, dB	Predicted ΔPWL, dB
				-90° 0°	0° 90°	Avg		
1	3	2740	0	- 6.2	- 4.6	- 5.4	BAD	-9.7
2	3	2740	0.3	- 8.0	-16.0	-12.0	BAD	-11.5
3	3	2740	0.2	-12.0	- 9.0	-10.5	BAD	-32
4	2	2740	0.2	- 1.3	- 0.4	- 0.9	- 3.7*	- 4.7
5	0	2740	0.2	- 3.8	- 3.6	- 3.7	- 7.3*	- 4.8
6	3	1570	0.2	- 3.2	- 5.8	- 4.5	- 7.0	- 3.9
7	0	1570	0.2	- 0.9	- 1.6	- 1.2	- 1.45	- 1.0
8	3	2150	0.2	- 2.5	- 1.8	- 2.1	- 6.9	- 3.1
9	0	2150	0.2	- 3.8	- 4.3	- 4.1	- 2.8	---
10	3	3250	0.2	- 3.5	- 9.4	- 6.4	- 6.3	- 3.0
11	0	3250	0.2	- 2.0	- 1.8	- 1.9	BAD	---

*Measurement Accuracy Questionable

Table VI. Summary of Predicted and Measured Suppression, Configuration 4

Run Number	Spinning Mode Order	Frequency, Hz	Mach Number	Far-field ΔPWL, dB			In-Duct Modal Meas ΔPWL, dB	Predicted ΔPWL, dB
				-90° 0°	0° 90°	Avg		
1	3	2740	0	- 4.5	- 3.8	- 4.2	-12.1	- 8.8
2	3	2740	0.3	Case Not Run				---
3	3	2740	0.2	- 6.5	- 7.3	- 6.9	BAD	-25.8
4	2	2740	0.2	Case Not Run				---
5	0	2740	0.2	- 1.7	- 2.75	- 2.2	- 8.4*	---
6	3	1570	0.2	- 7.8	-10.3	- 9.1	- 9.4	-10.5
7	0	1570	0.2	- 0.1	- 1.25	- 0.7	- 2.1	- 3.7
8	3	2150	0.2	- 6.6	- 3.9	- 5.3	- 9.6	- 7.0
9	0	2150	0.2	- 1.8	- 2.4	- 2.1	- 2.7	- 4.8
10	3	3250	0.2	- 6.8	-14.2	-10.5	- 7.9	- 3.0
11	0	3250	0.2	- 4.3	- 3.5	- 3.9	- 3.6	- 6.8

*Measurement Accuracy Questionable

Table VII. Summary of Predicted and Measured Suppression, Configuration 5

Run Number	Spinning Mode Order	Frequency, Hz	Mach Number	Far-field ΔPWL, dB			In-Duct Modal Meas ΔPWL, dB	Predicted ΔPWL, dB
				-90° 0°	0° 90°	Avg		
1	3	2740	0	-3.1	-2.9	-3.0	-15.0*	---
2	3	2740	0.3	Case Not Run				---
3	3	2740	0.2	-5.0	-6.2	-5.6	-18.4	-23.0
4	2	2740	0.2	Case Not Run				---
5	0	2740	0.2	-5.4	-6.6	-6.0	- 5.6	- 3.9
6	3	2740	0.2	+3.2	-2.3	+0.48	- 9.4	- 3.4
7	0	1570	0.2	-2.5	-3.4	-2.9	- 1.4	- 1.25
8	3	2150	0.2	-2.8	-2.4	-2.6	- 5.2	- 4.4
9	0	2150	0.2	-1.0	-2.4	-1.7	- 1.7	- 4.4
10	3	3250	0.2	-2.6	-7.25	-4.9	- 3.2	- 2.0
11	0	3250	0.2	+0.71	+1.15	+0.9	BAD	- 1.6

*Measurement Accuracy Questionable

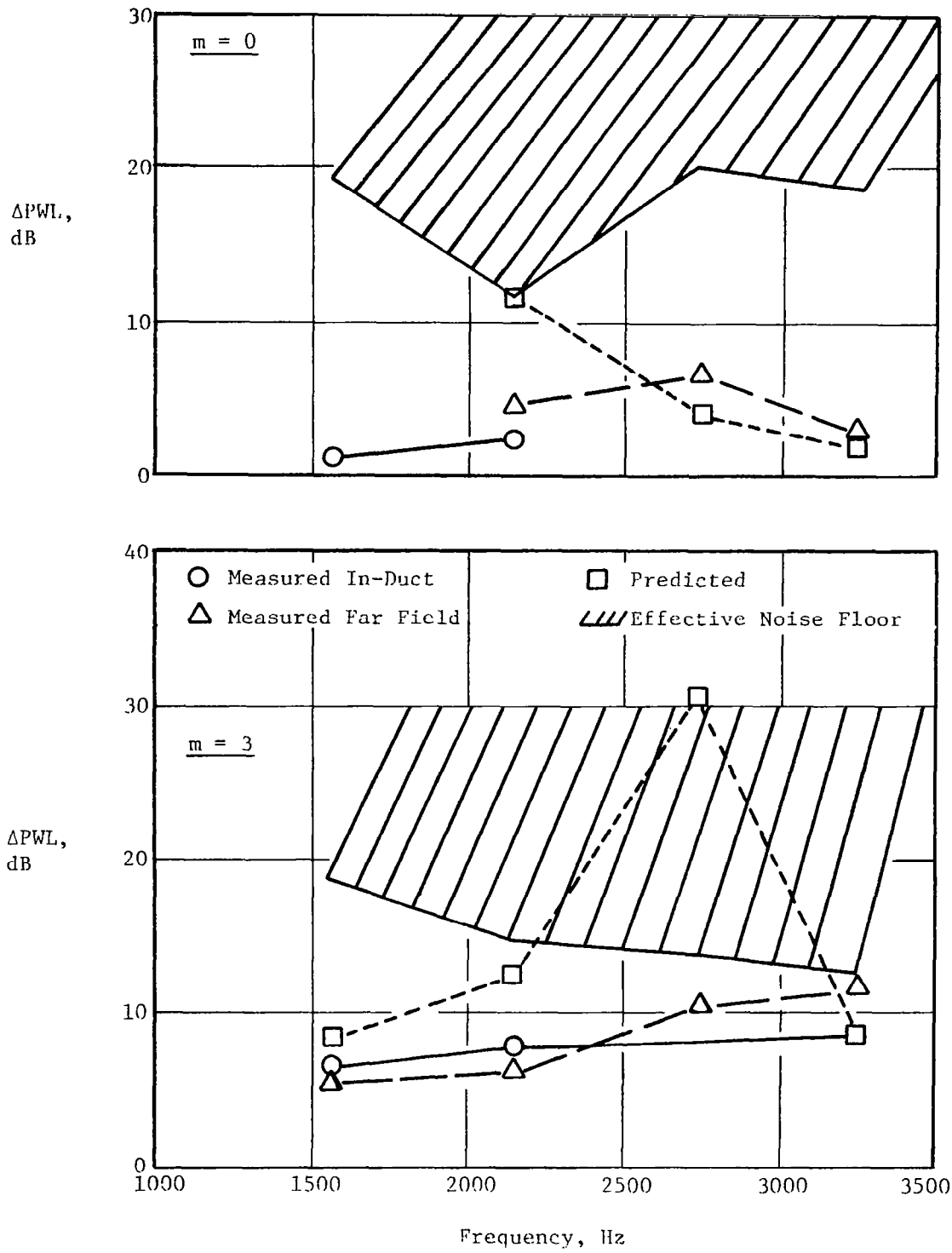

Figure 34. Comparison of Predicted and Measured Suppression, Configuration 2, Mach 0.2.

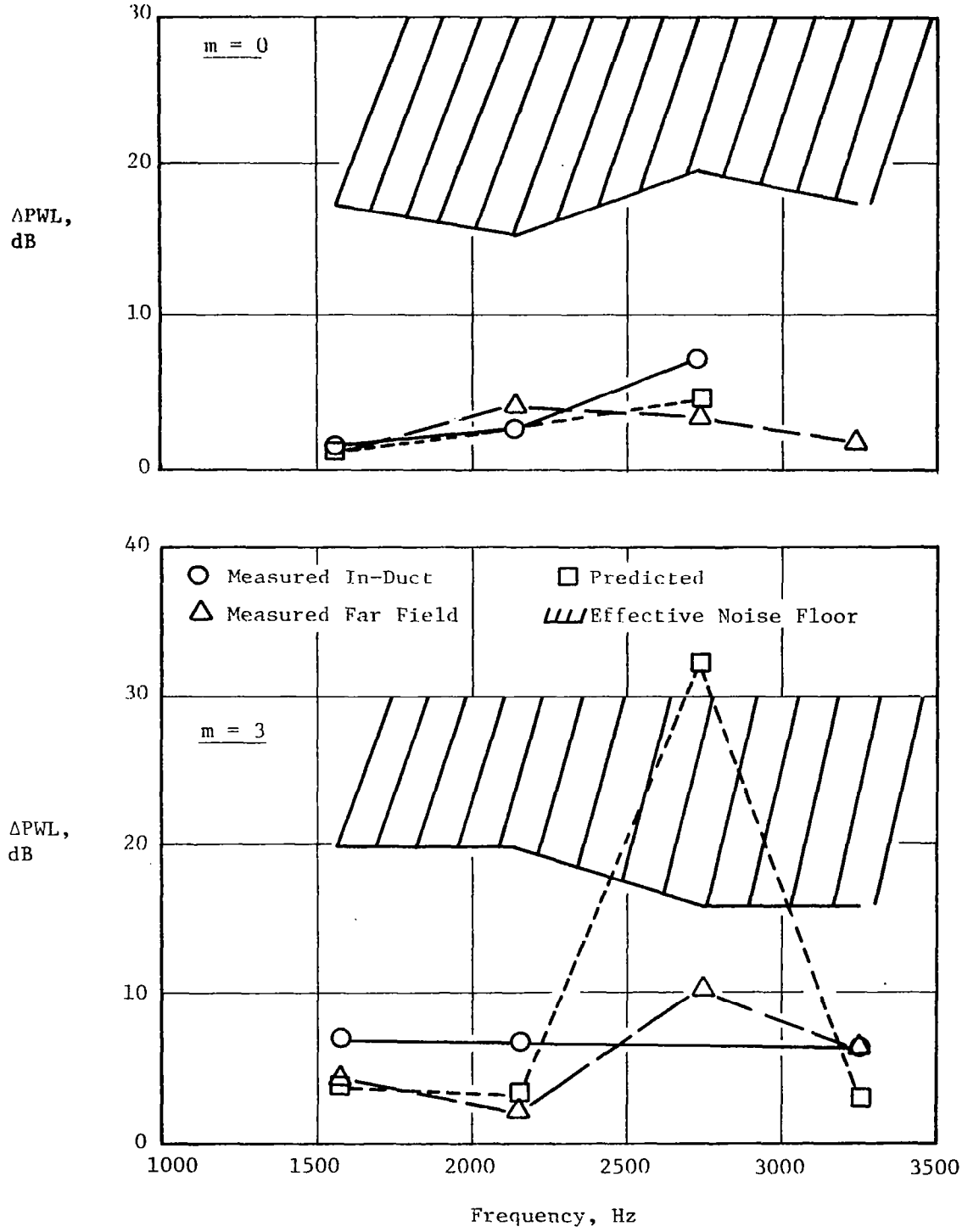

Figure 35. Comparison of Predicted and Measured Suppression, Configuration 3, Mach 0.2.

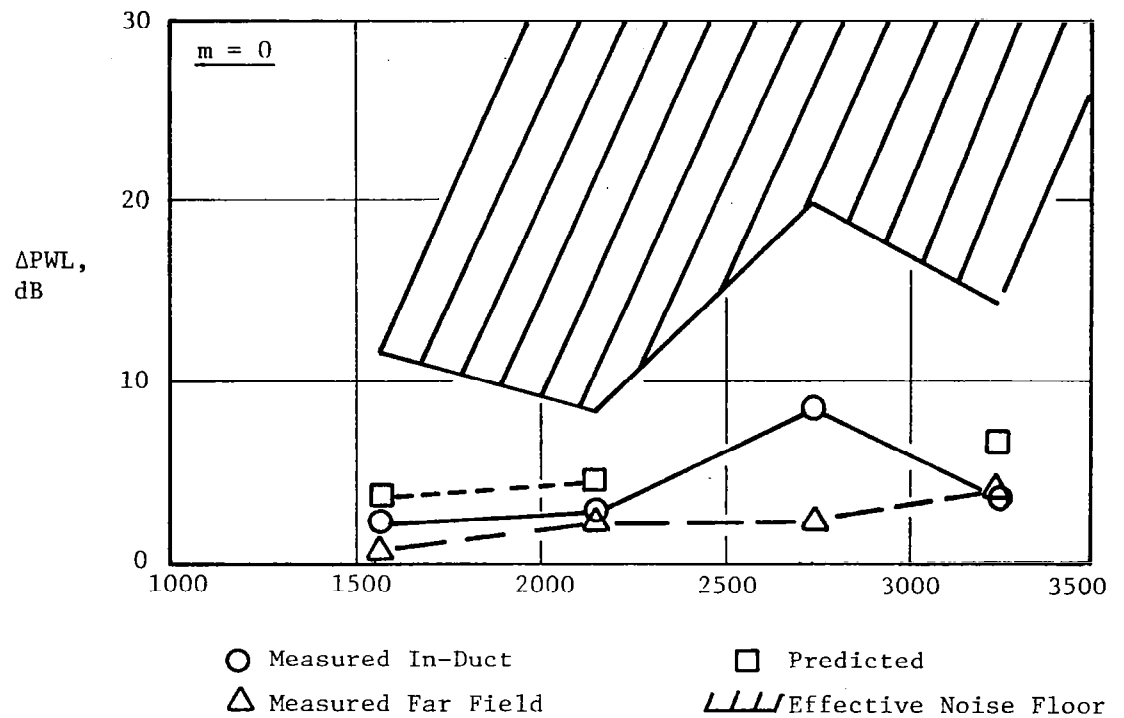

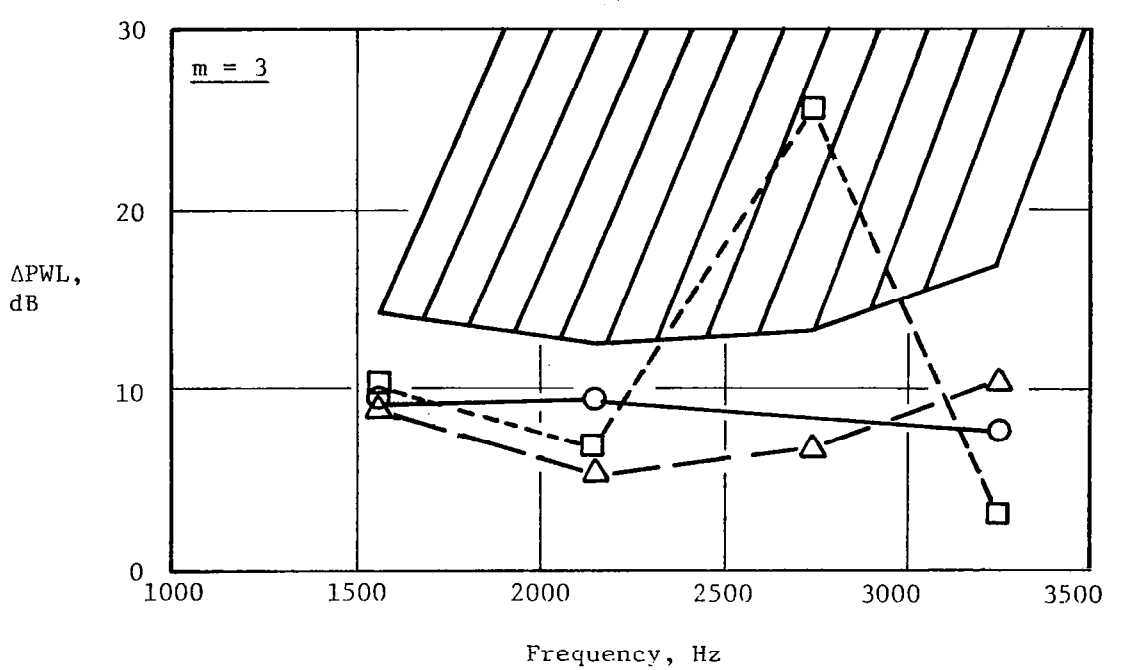

Figure 36. Comparison of Predicted and Measured Suppression, Configuration 4, Mach 0.2.

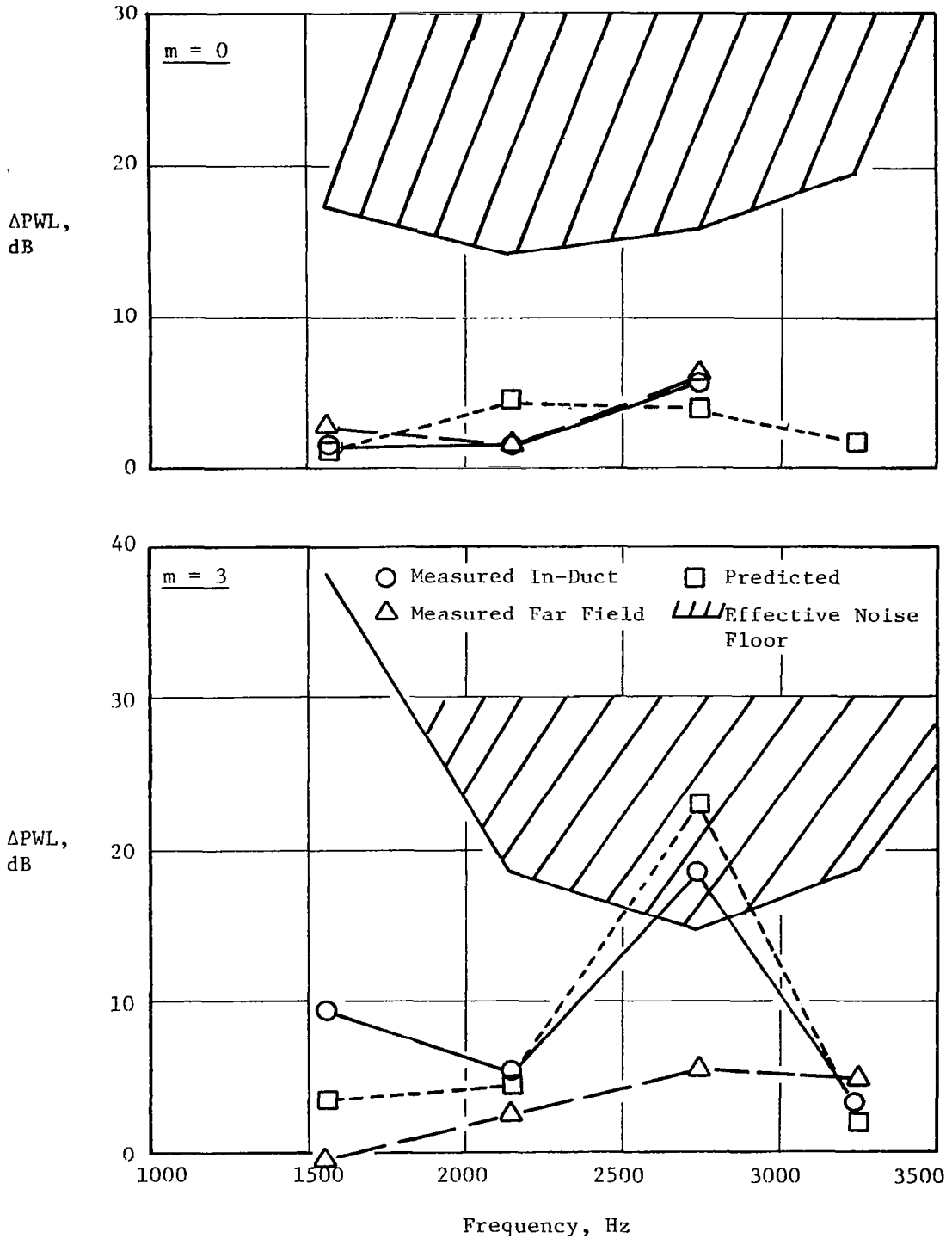

Figure 37. Comparison of Predicted and Measured Suppression, Configuration 5, Mach 0.2.

this can be obtained from the in-duct spinning-mode measurement downstream of the treatment. For each of the four treated configurations, the m = 0 spinning mode was found to be at the following relative levels below the m = +3:

Configuration 2-3: -13.5 dB
Configuration 3-3: -16.0 dB
Configuration 4-3: -13.6 dB
Configuration 5-3: -17.8 dB

Since the m = 0 mode attenuates at a much lower rate than the m = +3, it controls the total suppression and accounts for most of the energy measured at the upstream, in-duct, measurement plane and in the far field. That the m = 0 mode dominates the suppressed signal can be observed from the Run 3 plots of the far-field continuous traverses, Figures 30 through 33, where the central lobe at 0° is seen to dominate.

The ΔPWL's from the in-duct modal measurements were obviously in error for Run 3 of Configurations 2, 3, and 4, and the results are questionable for Configuration 5. The cause, again, is the presence of the m = 0 spinning mode. The data reduction technique expands the radial pressure profiles in terms of only m = +3 radial modes; thus, it is not using the modes which are actually present in the signal.

At the off-design conditions for the m = +3, Mach 0.2 cases (Runs 6, 8, and 10), the errors from this source are not nearly as great. There are two reasons for this: first, the m = 0 mode is at least -19.5 dB below the m = +3 levels as measured by the spinning mode probe; second, at off-design the suppression of the m = +3 mode is not great enough to take its energy level below the m = 0. This can be confirmed by examining the far-field continuous traverses for these cases, in which the m = +3 side lobes are seen to dominate the central lobe.

The Mach 0.0 cases, Run 1, also suffer from an m = 0 spinning mode contamination problem. In these cases, the predicted suppression is 3 to 5 dB above that measured in the far field. The in-duct measured suppression is higher than the predicted, but these measured values are probably in error, based on examination of the detailed modal measurement data.

In the remaining cases, the predicted and measured suppressions compare quite closely, with some exceptions. A fairly wide variation is found among the measured suppression values themselves, comparing both in-duct to far field and, in some cases, the far-field values measured over both quadrants.

The in-duct measurement was found to be quite sensitive to measurement parameters such as speed of sound and distance between measurement planes. This was true particularly for cases in which the data looked questionable, as evidenced by either energy calculations which indicated higher backward-traveling energy than forward-traveling or artificially enhanced levels for certain forward and backward radial mode orders, with a 180° phase difference. This enhanced level symptom is known to be caused by numerical problems in

the Mach 0.0 case, where the forward and backward modes have the same axial wavelength, under conditions where the separation of the measurement planes is an integral number of half-wavelengths of that mode. With mean flow, however, the axial wavelengths of the forward and backward modes are different so that, although the symptoms are the same, the causes are different. The exact cause of this phenomena was not discovered, and will require further investigation.

In the far-field measurement, several effects can be causing the lack of symmetry in the far-field radiation patterns and resulting suppression calculations. First, the presence of circumferential standing-wave patterns at the inlet entrance plane (radiation exit) could cause asymmetrical far-field radiation patterns in the azimuthal direction. This would happen only for higher spinning-mode orders for which both the positive and negative spinning modes were present in roughly equal amounts. The measurements in Figures 25 to 29, however, show the positive dominant spinning modes to be much higher than the negative modes of the same order, so that this cause is unlikely. A more likely source is the behavior of the anechoic chamber itself. For a pure-tone signal, even small reflections are likely to set up standing-wave patterns within the chamber. Preliminary measurements by Dr. Joe Posey of NASA-Langley, who traversed the far-field boom in the presence of a pure-tone point source, did indicate the presence of standing-wave patterns with up to 4 dB of variation which could lead to measurement errors.

The analytical predictions are subject to two predominant sources of error. First, errors in the experimental determination of the radial-mode content of the source will lead to errors in the prediction, particularly in cases where several radial modes are cut-on. Examination of the measured data indicated that errors of this nature should not have caused problems for any cases in this study since, for the m = 3 spinning mode, only one radial mode is cut-on. Second, errors in the prediction can be caused by incorrect values for the treatment impedance. This source of error will have its greatest effect near the optimum case, where suppression is most sensitive to impedance. Suppression predictions were made for Configuration 2, Run 3, in which the resistance and reactance were varied ±10% about the nominal value. The results, listed in Table VIII, indicate a variation from a minimum of 22.8-dB suppression to a maximum of 32.6 dB. These values still exceed the measured suppression values by a considerable amount, so this source of error cannot be the major reason for the discrepancy. At the off-design conditions, the variation of predicted suppression with impedance should be much smaller.

In several cases, the agreement among predicted and measured suppression can be considered to be excellent. One such example is Configuration 4, Run 6. This is the 5.1-cm (2-inch) + 5.1-cm (2-inch), two-panel Kevlar treatment at m = 3, 1570 Hz, Mach 0.2. This case is characterized by a spinning mode probe measurement which indicates the m = 0 mode to be 26.1 dB below the m = +3, a continuous far-field traverse with no strong central lobe, and an in-duct measurement with no sign of problems such as high backward-traveling energies either upstream or downstream. In this case, the measured and predicted values all agree within 2 dB at a ΔPWL of about 10 dB.

Table VIII. Variation of Predicted Suppression with Treatment Panel Impedance, Configuration 2, Run 3

$Z/\rho c$	ΔPWL, dB
1.04-1.44i (Nominal)	-30.8
1.04-1.58i	-22.8
1.04-1.30i	-27.3
1.14-1.44i	-32.6
0.94-1.44i	-24.2

Thus, when all conditions are correct, both the advanced measurement techniques and the prediction are successful. Discrepancies which are present are caused by the extreme experimental difficulties in establishing and measuring the conditions under which the prediction program is valid. These problems can be overcome by further advancements in experimental technique development and further refinements to the analysis.

6.3 EVALUATION OF TREATMENT PERFORMANCE

Evaluation of the treatment performance at the design condition (Run 3, m = 3, 2740 Hz, Mach 0.2) is, unfortunately, very difficult to make, due to the experimental problems encountered in this case. The measured far-field suppression values follow the same trend as the predicted values, but are about 20 dB below them. The major objectives here were to compare ostensibly equivalent bulk absorber and SDOF designs under the same conditions and compare 4-inch single-phase Kevlar with 2-in single-phase Kevlar.

The measured values from Run 3 show the performance of the 10.2-cm (4-inch) single-phase Kevlar (Configuration 2) and the 10.2-cm (4-inch) single-phase SDOF (Configuration 3) to be about the same, with the possible exception of 3250 Hz, where the Kevlar panel gives higher suppression. This is the result which would be expected based on theory, which states that two panels of different design but with the same impedance values should give the same results. The primary difference between the two panel designs should occur as a result of the non-linear behavior of the SDOF panel, because impedance will vary with mean flow Mach number or high-intensity sound levels. Differences between Configurations 2 and 3 at off-design run conditions are caused by the differences in impedance (as listed in Table III), as evidenced by the predicted suppressions. The higher suppression of the Kevlar panel at the high test frequency (3250 Hz) compared to the SDOF panel cannot be attributed to the high-frequency improved suppression performance usually expected from bulk absorber panels. This effect is caused by the reactance of the bulk absorber panels staying close to zero at frequencies where the SDOF panel achieves high positive values. At 3250 Hz, the SDOF panel is actually more negative than the Kevlar panel in reactance, having gone through a branch of the cotangent curve.

Comparisons among Kevlar Configurations 2, 4, and 5 are more inconclusive, due to the scatter in the data. At the design condition (Run 3), the 5.1-cm (2-inch), single-phase gives about 3.5 dB less measured suppression than the 10.2-cm (4-inch), single-phase, and the two-element treatment (2+2) configuration gives less than either single-element (as predicted) configuration. Under the conditions of Run 6 (m = 3, 1570 Hz, Mach 0.2), the 5.1-cm (2-inch) does slightly better than the 10.2-cm (4-inch) Kevlar, as predicted, but the 5.1-cm+5.1-cm (2+2-inch) results are questionable. For Runs 8 and 9 the measured suppressions are all similar, but the predicted suppression for Configuration 2 is too high. Scatter makes Runs 5 and 10 difficult to interpret, and all suppression values are very low in Runs 7 and 11.

Generally, it can be concluded that the suppression performance of the treatment panels conforms reasonably well with the prediction. Under the design conditions of this study, the use of conventionally designed multiphase liners was not apropos, but the design of the single-phase, optimum liner is quite sensitive to the effects of the boundary layer and, in fact, uses the acoustic influence of the boundary layer to create a phasing effect between the treatment and the upstream hard-wall length of the duct, increasing the effective treated L/D.

7.0 CONCLUSIONS AND RECOMMENDATIONS

The eigenvalue calculation routine for the cylindrical duct has been modified such that it will successfully find the correct sequence of eigenvalues for an arbitrary wall impedance in the presence of uniform mean flow. The occurrence of double eigenvalues and missed eigenvalues has been eliminated for all cases run to date. The calculation for the eigenvalues in the presence of a boundary layer has proven to be successful in over 90% of the cases, with the occasional occurrence of a numerical convergence problem. Further study is needed to investigate the causes of the numerical problems for those cases in which the boundary-layer-effects eigenvalue routine fails to converge.

In the inlet case, the boundary layer effects have significant influence on the design of the optimized treatment. Although conventional, multiphased treatment designs offer no significant suppression enhancement at the η-values which were considered for this study, the boundary layer effects cause single-phase treatment designs to act in what might be considered an unconventional, or limited, multiphase manner in conjunction with upstream hard-wall lengths of duct such that significant amounts of energy are absorbed in the hard-wall section. The treatment acts to establish a wave modal pattern which can be efficiently attenuated in the hard-wall duct with a boundary layer (which is essentially a phasing effect), increasing the effective treatment L/D ratio. The results of the study demonstrate that high suppressions can be obtained using this effect with very short treatment lengths: in this case, as low as a 0.167 ratio of treated length to duct diameter.

Due to experimental difficulties in establishing pure spinning-mode source patterns, the high suppressions predicted for the optimum designs for the four treatment configurations were not obtained from the tests. Sufficient evidence was obtained from the off-design cases, however, to demonstrate that prediction and measurement will agree quite closely under ideal test conditions. Measurement problems were experienced for both the in-duct and far-field suppression measurement methods, making evaluation of the data difficult in some cases.

The development of the forward/backward-wave separation technique in the cylindrical duct represents an initial attempt at applying this advanced data acquisition/reduction technique to an in-duct measurement. When the conditions of measurement matched the analytical assumptions of the measurement method, the measurement successfully separated forward and backward modes. However, the method is not without experimental difficulties; under certain conditions, the results are quite sensitive to the input parameters and yield obviously incorrect mode and energy levels. Further development of the method is needed in the form of extensive testing in hard-wall ducts with and without flow under a wide variety of frequency and source-mode conditions. By increasing the number of circumferential locations of radial probe traverses at each plane, the presence of multiple spinning-mode orders could be taken into account.

Under equivalent conditions, both the Kevlar bulk absorber and the SDOF panels gave nearly the same suppression. Differences in suppression at the design and off-design conditions can be explained by differences in impedance among the panels.

In addition to the above-mentioned areas for further research, it would be useful to conduct a more thorough computer investigation of the effects of the boundary layer on inlet suppression and optimized treatment design. The boundary layer effects in this study are based on a simplified profile assumption and could be easily extended to an arbitrary profile shape. The numerical procedure for calculating the boundary layer effects is relatively lengthy and expensive, and further work in this area could lead to increases in speed, reliability, and efficiency.

In general, the program must be construed as an exploratory investigation into a number of advanced methods of analysis and measurement techniques for increasing our understanding of treatment design and performance in inlet ducts. The method of in-duct, forward/backward-wave separation is an exacting measurement technique which requires some further development to realize its full potential, particularly in reference to the in-duct impedance measurement method. The in-duct spinning-mode measurement was highly successful and provided critical information for the interpretation of the test results of this program. The analytical prediction program is reliable and in its current form provides an outstanding tool for inlet treatment design.

8.0 REFERENCES

1. Zorumski, W., "Acoustic Theory of Axisymmetric Multisectioned Ducts," NASA TR R-419, May 1974.

2. Nayfeh, A.H., Kaiser, J.E., Shaker B.S., "Effect of Mean Velocity Profile Shapes on Sound Transmission Through Two-Dimensional Ducts," Journal of Sound and Vibration, Vol. 34, No. 3, June 1974, pp 413-423.

3. Kraft, R.E., "Theory and Measurement of Acoustic Wave Propagation in Multi-Segmented Rectangular Flow Ducts," Ph.D. Dissertation, University of Cincinnati, June 1976; also, General Electric Report No. R77AEG585, October 1977.

4. Motsinger, R.E., Kraft, R.E., et al, "Optimization of Suppression for Two-Element Treatment Liners for Turbomachinery Exhaust Ducts," NASA CR-134997, April 1976.

5. Rice, E.J., "A Method for the Acoustic Impedance of a Perforated Plate Liner with Multiple Frequency Excitation," NASA TMX-67950, October 1971.

6. Motsinger, R.E., Kraft, R.E., Paas, J.E.., Gahn, B.M., "Analytical and Experimental Studies of Acoustic Performance of Segmented Liners in a Compressor Inlet," NASA CR-2882, September 1977.